Trajectory optimization of a planetary sunshade around L1

Heiligers, M.J.; Oggionni, F.; Sanchez, Joan-Pau

Publication date
2022

Published in
Proceedings of the ASCEND 2022 Conference

Citation (APA)
Heiligers, M. J., Oggionni, F., & Sanchez, J.-P. (2022). Trajectory optimization of a planetary sunshade around L1. In *Proceedings of the ASCEND 2022 Conference*

Trajectory optimization of a planetary sunshade around the Sun-Earth L_1 point for solar geoengineering

Filippo Oggionni *
Faculty of Aerospace Engineering, Delft University of Technology

Jeannette Heiligers †
Faculty of Aerospace Engineering, Delft University of Technology

Joan-Pau Sanchéz ‡
ISAE-Supaero

A planetary sunshade is a large, reflecting disk built to shield the Earth from a small fraction of solar irradiance and partly compensate global warming caused by greenhouse gas emissions. As a specific form of solar geoengineering, the sunshade is an emergency solution that would be implemented to prevent catastrophic climate change, while working towards the net-zero emission goal. In this paper, a dynamic sunshade is proposed. The motion of the sunshade is designed as a combination of static permanence at two equilibrium points above and below the ecliptic plane to shade the poles and a time-optimal transfer trajectory to connect these equilibrium points without overshading the tropical regions. Such a system is capable of not only reducing the global mean surface temperature anomaly, but also minimizing regional climate changes by tailoring the sunshade's motion according to climate requirements, which is the primary goal of this work. A simplified climate model is used to evaluate the results of a given shading pattern, directly related to the sunshade's trajectory. A dynamic sunshade with a radius of 1434 km and orbiting in the vicinity of the Sun-Earth L_1 point is able to reduce the global mean surface temperature from 16.39°C (scenario with 680 ppm of atmospheric CO_2, double the amount with respect to the pre-industrial era) to 14.13°C until equilibrium is reached. It also reduces the polar mean surface temperature (for latitudinal bands above 65°) by more than 2°C with respect to a scenario without sunshade and by 0.06°C with respect to a static sunshade at the displaced L_1 point. The optimal results are achieved when the sunshade is located at a distance equal to 30% of the Earth's radius above and below the ecliptic plane. In addition, the transfers between the equilibrium points start respectively at day 56 and day 250, both measured from the 1st of January.

I. List of abbreviations

AEP	=	Artificial Equilibrium Point
AU	=	Astronomical Unit
CR3BP	=	Circular Restricted Three-Body Problem
EBM	=	Energy Balance Model
ECEF	=	Earth-Centered Earth-Fixed
ECI	=	Earth-Centered Inertial
EMIC	=	Earth Model of Intermediate Complexity
EOM	=	Equation of Motion
GDP	=	Gross Domestic Product
GHG	=	Greenhouse Gas

*MSc student, Department of Astrodynamics and Space Missions, Kluyverweg 1, 2629 HS Delft, The Netherlands – f.oggionni@student.tudelft.nl

†Assistant Professor, Department of Astrodynamics and Space Missions, Kluyverweg 1, 2629 HS Delft, The Netherlands – m.j.heiligers@tudelft.nl

‡Professor, ISAE-Supaero, avenue Édouard-Belin 10, BP 54032 - 31055 Toulouse CEDEX 4, France – Joan-pau.SANCHEZ@isae-supaero.fr

GMST	=	Global Mean Surface Temperature
GREB	=	Globally Resolved Energy Balance
IPCC	=	International Panel on Climate Change
IPOPT	=	Interior Point Optimizer
IRF	=	Inertial Reference Frame
LEO	=	Low Earth Orbit
LRF	=	Local Reference Frame
NLP	=	Non-Linear Programming
RCP	=	Representative Concentration Pathway
SRF	=	Synodic Reference Frame
SRP	=	Solar Radiation Pressure

II. List of symbols

Roman symbols

A	=	Area of the sunshade
$\mathbf{a}_{SRP}$	=	Solar radiation pressure acceleration vector
c	=	Speed of light
c_i	=	Coefficient of order i
d_r	=	Radial distance
F_X	=	Climate forcing due to X
h	=	Hour angle
$\lvert h_0 \rvert$	=	Hour angle at sunset/sunrise
I	=	Radiance
I_0	=	Radiance under fully illuminated conditions
I_{ae}	=	Radiance under annular eclipse conditions
I_c	=	Radiance emitted by the Sun at its center
I_{pe}	=	Radiance under partial eclipse conditions
I_r	=	Radiance emitted by the Sun at a radial distance d_r
J_1	=	Objective function for the optimal control problem
J_{RMS}, J_{GMST}	=	Objective functions for the heuristic optimization problem
$L\,(\hat{\mathbf{r}}_{13}, \hat{\boldsymbol{\zeta}}, \hat{\boldsymbol{\xi}})$	=	Local Reference Frame
m	=	Mass of the sunshade
m_1	=	Mass of the primary (Sun)
m_2	=	Mass of the secondary (Earth)
$\hat{\mathbf{n}}$	=	Vector normal to the sunshade
P	=	Solar radiation pressure
Q	=	Insolation
$\mathbf{r}$	=	Position vector of the sunshade in the SRF
$\mathbf{r}_1$	=	Position vector of the primary (Sun) in the SRF
$\mathbf{r}_2$	=	Position vector of the secondary (Earth) in the SRF
$\mathbf{r}_{13}$	=	Position vector of the sunshade with respect to the Sun
$\mathbf{r}_{23}$	=	Position vector of the sunshade with respect to the Earth
$\mathbf{r}_{A,B}$	=	Position vector of B with respect to A
$\bar{r}_{\oplus}$	=	Average Sun-Earth distance (1 Astronomical Unit)
$r_{\oplus}$	=	Varying Sun-Earth distance
R	=	Radius of a body
$\text{S}(\hat{\mathbf{x}}, \hat{\mathbf{y}}, \hat{\mathbf{z}})$	=	Synodic Reference Frame
S	=	Irradiance
S_0	=	Solar constant
T	=	Surface temperature
$\bar{T}$	=	Monthly mean surface temperature

$\bar{T}^{\text{global}}$ = Global mean surface temperature
$\bar{T}^{\text{polar}}$ = Polar mean surface temperature
t = Generic epoch
t_i = Start time of the transfer trajectory
$t_{i,N}$ = Start time of the transfer trajectory from above to below the ecliptic plane
$t_{i,S}$ = Start time of the transfer trajectory from below to above the ecliptic plane
U = Potential function of the CR3BP
$\mathbf{X}_1$ = State vector of the optimal control problem
$\mathbf{X}_2$ = Decision vector of the heuristic optimization problem
z_N = Vertical displacement of the AEP above the ecliptic plane
z = Vertical displacement of the AEP below the ecliptic plane

Greek symbols

α = Cone angle
β = Lightness number
γ = Solar angle corresponding to a radial distance d_r
δ = Clock angle
η = Angular separation between the Sun and the sunshade
θ = Cone angle
λ = Latitude angle
μ = Mass parameter of a CR3BP
ν = Declination angle
σ = Critical sail loading
τ = Surface albedo
φ = Longitude angle
χ_{clouds} = Cloud albedo
χ_{surf} = Surface albedo
ψ = Solar zenith angle
$\boldsymbol{\omega}$ = Angular velocity vector of the Earth around the barycenter of the Sun-Earth system
$\boldsymbol{\Omega}$ = Solid angle subtended by a body

Subscripts

$\square_D$ = Sunshade
$\square_{\text{geo}}$ = Geoengineered scenario
$\square_{\text{ref}}$ = Reference scenario
$\square_{\oplus}$ = Earth
$\square_{\odot}$ = Sun

Superscripts

$\hat{\square}$ = Unit vector
$\bar{\square}$ = Averaged quantity
$\dot{\square}$ = First derivative with respect to time
$\ddot{\square}$ = First derivative with respect to time
$\square^*$ = Relative quantity

III. Introduction

Climate change is one of the most pressing issues of the 21st century. As a matter of fact, the Fifth Assessment Report from the International Panel on Climate Change (IPCC) draws four different Representative Concentration Pathways (RCPs), outlining different climatic scenarios based on future, predicted emissions of greenhouse gases (GHG). These four scenarios would result in a globally averaged surface temperature anomaly between 1.0 °C and 4.0 °C by 2100 [1]. In Fig. 1, the temperature anomaly resulting from a step-like increase of CO_2 content (680ppm) is shown. Such a scenario, which will be explained in more detail in Sec. IV, results in a global surface temperature anomaly of approximately 2.5 °C, computed with respect to pre-industrial levels, and is in agreement with the two middle RCPs (RCP 4.5 and RCP 6.0) presented in Reference [1]. As a comparison, the most recent observations published by the National Ocean and Atmospheric Administration show that the atmospheric concentration of CO_2 has already reached

421 ppm*. In turn, a CO_2 concentration of 680 ppm could be reached already in 2055, according to the worst RCP predicted by the IPCC [1]. Policymakers and researchers are focusing on how to prevent catastrophic consequences on the Earth's ecosystems by reducing emissions of GHGs. In parallel, several methods to artificially modify the Earth's climate system have been proposed [2]. These methods are collectively known as *geoengineering* and they include both preventive (e.g., capturing CO_2 from the atmosphere [3]) and mitigation (e.g., solar geoengineering [4]) techniques. Geoengineering should be considered as a complementary set of methods to limit extreme climate consequences, while the international community works towards the goal of net-zero emission, and to prevent the climate system from reaching tipping points that would result in irreversible cascade effects [5]. So, by all means, geoengineering should not be considered as a substitute of GHG emission reduction policies. However, the little amount of research conducted on geoengineering is still insufficient to conduct a proper assessment of its effects.

In this paper, only solar geoengineering is considered. Solar power is the main source of forcing in the Earth's climate system. The basic principle of solar geoengineering consists of blocking a fraction of the solar radiative flux reaching the Earth with the ultimate goal to offset the Earth's global energy balance. This solution would in principle allow to create and maintain an artificial climate system with increased atmospheric CO_2 content, balanced by lower levels of incoming solar radiation [6]. It should be mentioned that solar geoengineering not only has benefits. In the first place, it does not address the issue of ocean acidification. Secondly, it poses the risk of the so-called *termination effect*: this effect, particularly valid for space-based systems, refers to the possibility of returning to the natural solar irradiance levels very quickly, following an unexpected and sudden failure of the solar geoengineering system. This circumstance would result in a rapid rise in surface temperature. A broad survey collecting the opinion on space-based geoengineering of 125 experts in the field was conducted in Reference [7].

Previous studies analyzed the climate changes occurring with increased CO_2 levels and a subsequent reduction in the solar constant, focusing on the effects on the global surface temperature [8, 9], on its regional differences [10–12], on the hydrological cycle [13, 14], and on the transient climate dynamics [15]. Methods and techniques to minimize climate anomalies were also proposed [16–18]. Other studies treated the topic of a planetary sunshade in more detail, first exploring the concept in a general manner [19, 20], then focusing on the mission requirements [21] and on alternative mission architectures [22–25]. More in-depth studies researched several aspects of a space-based geoengineering mission: the sunshade's optimal location [6, 26], logistical challenges [27], orbit control techniques [28], spectrally selective materials for its fabrication [29], a possible roadmap towards its implementation [30], and its costs [31]. In particular, the latter study claims that, if the sunshade system has a mass smaller than 100 Mt and simultaneously ensures an insolation reduction of at least $0.8\,Wm^{-2}$ from 2050 to 2150, the economic costs of climate change caused by a $2xCO_2$ scenario can be reduced by 240 billion USD from roughly 500 billion USD.

The vast majority of the studies concerned with space-based geoengineering focused on the concept of a static sunshade, continuously located at the displaced L_1 point. On the other hand, a considerable amount of climate studies consider a spatially and temporally distributed reductions in solar irradiance. Indeed, it was demonstrated extensively

*https://www.noaa.gov/news-release/carbon-dioxide-now-more-than-50-higher-than-pre-industrial-levels, accessed on 10th September 2022

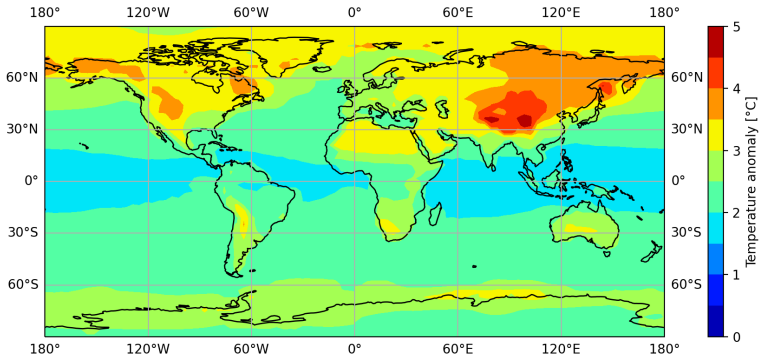

Fig. 1 Surface temperature anomaly after 50 years resulting from an instantaneous increase of atmospheric CO_2 to 680ppm. The simulation was performed with the GREB climate model; for more details, see Sec. VII.

by climate scientists that a static sunshade (corresponding to a spatially and temporally uniform reduction in solar irradiance) produces overcooling in tropical regions and undercooling in polar regions [32]. If a dynamic sunshade is adopted, its trajectory can be tailored to selectively shade different latitudinal bands on the Earth depending on the day of the year. In particular, a slightly greater reduction in insolation should be achieved over the polar regions and a slightly smaller reduction over the tropics. Furthermore, there are very few studies that treat both the trajectory design and its impact on the climate simultaneously. The two aspects are tightly coupled, since the motion of the sunshade has a direct effect on the reduction of solar irradiance and thus on the climate. This coupling is particularly important when regional climate changes are accounted for.

This work aims to fill these research gaps by assessing whether a large, dynamic (i.e., capable of orbiting above and below the ecliptic plane) sunshade is capable of minimizing residual climate changes arising in the Earth's climate system with increased atmospheric CO_2 (680 ppm, twice the amount with respect to pre-industrial levels). It does so by evaluating the performance of the sunshade's trajectory in the vicinity of the L_1 point with a simplified climate model, which allows to account for the artificial solar irradiance distribution generated by a dynamic sunshade.

So far, only one study investigated the trajectory design of a dynamic sunshade to minimize residual regional climate changes [33]. In that study, a reverse-engineering approach was used to find optimal periodic orbits around the L_1 point to tune the trajectory of the sunshade to the seasonal variations in the Earth's climate. This is achieved by linearly combining a set of static solutions with a non-zero displacement with respect to the ecliptic plane and subsequently connecting those solutions to create a periodic orbit.

In this work, a different approach, explained in Sec. IV, is proposed. Instead of using periodic orbits, a combination of equilibrium positions and time-optimal transfer between such equilibrium positions is used. The trajectory of the sunshade is controlled through the solar radiation pressure acceleration, the dynamical framework of which is presented in Sec. V. The shade cast on the Earth is computed with high accuracy (Sec. VI) and the artificial solar irradiance distribution is fed to a simplified climate model, presented in Sec. VII. The numerical methods used to optimize the motion of the sunshade are presented in Sec. VIII, while the results are discussed in Sec. IX. Conclusions are drawn in Sec. X.

IV. Problem Definition and Methodology

The approach used in this work to optimize the sunshade's trajectory is illustrated in Fig. 2. The trajectory over one year is composed of two separate parts: 1) the sunshade is alternately *parked* at two equilibrium points (one above the ecliptic plane during the summer and one below during the winter) and 2) the sunshade is transferred between the two equilibrium points (one transfer during spring and one during fall). As mentioned, the sunshade is placed below the ecliptic plane during the northern hemisphere winter and above the ecliptic plane during the northern hemisphere summer. This is done to ensure a greater reduction of insolation over the poles during local summer, while at the same time avoiding an excessively large insolation reduction over the equatorial regions. For most of the time during the year, the sunshade is located at either equilibrium points, which are in fact Artificial Equilibrium Points (AEPs): these equilibria are enabled by a given attitude of the sunshade [34, 35]. A formal definition of AEPs will be given in Sec. V.

The AEPs are connected by a time-optimal transfer trajectory. The transfer time is minimized to avoid overshading (and thus overcooling) of the equatorial regions. At a specific date during the northern hemisphere spring, the sunshade is transferred from an AEP below the ecliptic plane to an AEP above the ecliptic plane. After that, at another given date during the northern hemisphere fall, the same transfer is repeated. The details of the optimal control problem to find a minimum-time transfer trajectory are explained in Sec. VIII.A. The location of the AEPs, together with the departing dates of the transfer trajectory, are the independent variables that will be optimized in this work.

The insolation distribution resulting from the presence of the sunshade has both a temporal and a spatial dependency; however, in this paper, the spatial dependency is limited to latitudinal variations. This assumption is justified by the fact that longitudinal variations are relevant only if a sub-daily temporal resolution is required, yet this is not the case for this work. The artificial insolation distribution is then fed to a climate model (GREB), described in Sec. VII. The GREB model simulates surface temperatures on a regular grid of nodes, separated by 3.75° in latitude and longitude, based on a simplified global energy balance [36]. The insolation distribution derived from the presence of the sunshade is repeated for each year throughout the GREB simulation, which lasts for 50 years. Finally, the temperature anomalies are evaluated at the final year of the simulation and compared to a reference scenario corresponding to pre-industrial levels of atmospheric CO_2 and with a nominal solar radiation distribution [36]. The reference scenario is also computed by GREB with a 50-year-long climate simulation.

A few assumptions are made; assumed values of some quantities are reported in Table 1. The main sizing parameters

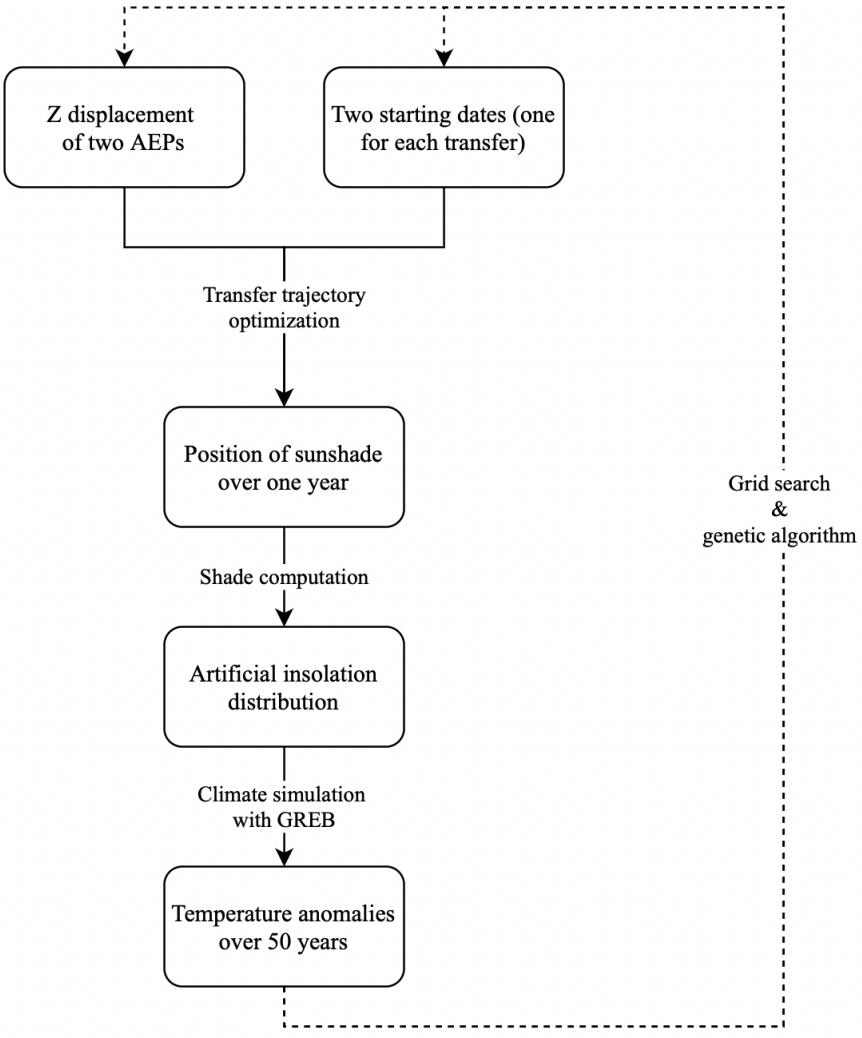

Fig. 2 Schematics of the methodology used in this work and described in Sec. IV.

for a static sunshade are its radius R_D and its distance from the Earth $r_{D,\oplus}$, which directly affect the mass of the sunshade. The minimization of the sunshade's mass, for a static sunshade located in the ecliptic plane along the Sun-Earth line, has been explored thoroughly in literature [6, 19, 20, 33]. Therefore, the values found in Reference [33] for the Earth-sunshade distance along the Sun-Earth line (as reported in Table 1) are adopted in this work. For a static sunshade with parameters as in Table 1, such assumptions ensure a global reduction in insolation of 1.7%, which has been proved as the minimum value to balance the climate effects of a doubling of the atmospheric CO_2 with respect to pre-industrial levels [6]. With respect to published work, in this paper the out-of-plane displacement of the sunshade is non-zero. However, the global insolation reduction obtained in this work will not differ significantly from 1.7%, since the out-of-plane component of the sunshade's location with respect to the Earth is roughly three orders of magnitude smaller than the Earth-sunshade distance. The upper limit placed on the out-of-plane displacement is derived by the fact that for a large out-of-plane displacement most of the shade would not be cast on the Earth. As a result, the in-plane AEP found in Reference [6] will be considered as a starting point. More details of the geometry of the system and on the AEPs are provided in Sec. V.

To select the optimal out-of-plane displacement of the AEPs and the dates on which the orbital transfers should be initiated, two methods are used in this paper: a grid search to explore the search space and a genetic algorithm. The settings used for the heuristic optimization are described in Sec. VIII.B, while the results are discussed in Sec. IX.

Table 1 Characteristic quantities for the sunshade and the climate model assumed in this work.

Quantity	Notation	Value	Unit	Source
Radius of the sunshade		1434	km	[33]
Distance of the sunshade from the Earth		$2.44 \cdot 10^6$	km	[33]
Pre-industrial levels of atmospheric CO_2		340	ppm	[36]

V. Dynamical Model

In this section, the dynamical model is presented in detail. The framework of the Circular Restricted Three-Body Problem is explained, together with the perturbing solar radiation pressure acceleration. The notation, reference frames, and the equations of motion are formulated in Sec. V.A. The section then focuses on the solar radiation pressure acceleration and how it can be exploited to control the orbital motion of the sunshade (Sec. V.B). Finally, the associated equilibrium solutions are discussed in Sec. V.C.

A. Circular Restricted Three-Body Problem

In this paper, the motion of the sunshade is designed in the framework of the Sun-Earth Circular-Restricted Three-Body Problem (CR3BP). It is therefore assumed that the sunshade is subject to the point-mass gravitational attraction of the primaries – the Sun (m_1) and the Earth (m_2) – neglecting the gravitational attraction of other celestial bodies in the solar system. In addition, since the mass of the sunshade, m, is negligible with respect to the mass of the primaries, the gravitational attraction exerted by the sunshade on the primaries is not considered [37]. Finally, the motion of the primaries around the barycenter of the system is assumed to be circular.

To describe the motion of the sunshade, a synodic (or corotating) reference frame (SRF), S($\hat{\mathbf{x}}$, $\hat{\mathbf{y}}$, $\hat{\mathbf{z}}$), is introduced. The SRF, visualized in Fig. 3, is centered at the barycenter of the Sun-Earth system, O. One axis of the SRF, $\hat{\mathbf{x}}$, coincides with the vector connecting the primaries and is always oriented towards the smaller primary, m_2, while the $\hat{\mathbf{z}}$-axis coincides with the constant angular velocity vector, $\boldsymbol{\omega}$, describing the circular motion of m_1 and m_2 around the barycenter. The $\hat{\mathbf{y}}$-axis completes the right-handed reference frame. The position vectors of the Sun and the Earth in the SRF are denoted with $\mathbf{r}_1$ and $\mathbf{r}_2$, respectively, and the position of the sunshade with $\mathbf{r} = [x \quad y \quad z]^T$.

Under the assumptions presented in Sec. V.A, it is possible to describe the motion of the sunshade in the CR3BP in non-dimensional form by introducing new units of mass ($m_1 + m_2$), length ($|\mathbf{r}_1| + |\mathbf{r}_2|$), and time ($2\pi|\boldsymbol{\omega}|^{-1}$). The characteristic parameter μ is also introduced:

$$\mu = \frac{m_2}{m_1 + m_2} \tag{1}$$

For the Sun-Earth system, this yields $\mu = 3.041464 \cdot 10^{-6}$ [38, 39]. As a result, the motion of the sunshade in the

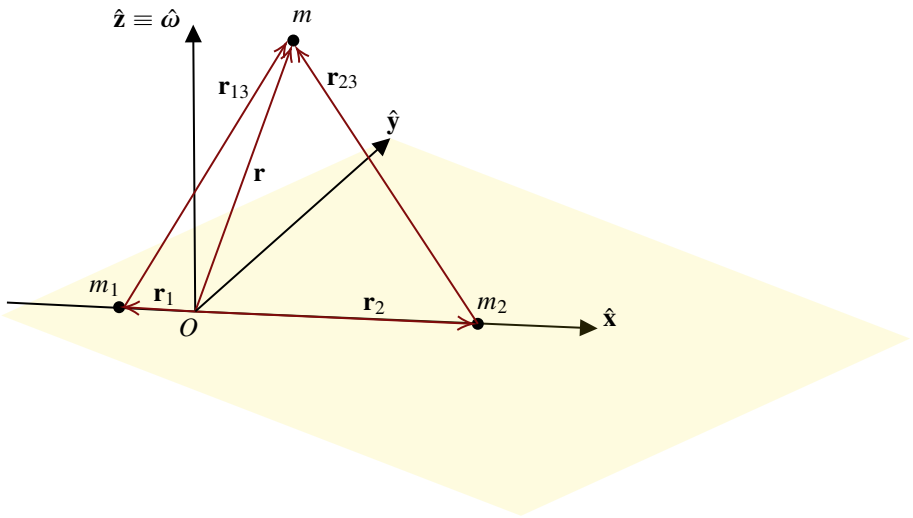

Fig. 3 The bigger primary (m_1), the smaller primary (m_2), and the planetary sunshade (m) represented in the synodic reference frame, S($\hat{\mathbf{x}}$, $\hat{\mathbf{y}}$, $\hat{\mathbf{z}}$).

synodic reference frame expressed in dimensionless quantities is described as [37]:

$$\ddot{\mathbf{r}} = -\left(\frac{1-\mu}{r_{13}^3}\mathbf{r}_{13} + \frac{\mu}{r_{23}^3}\mathbf{r}_{23}\right) - 2\,\boldsymbol{\omega} \times \dot{\mathbf{r}} - \boldsymbol{\omega} \times (\boldsymbol{\omega} \times \mathbf{r}) + \mathbf{a}_{SRP} \tag{2}$$

where $r_{\square} = |\mathbf{r}_{\square}|$. The first and second derivatives are denoted with single and double dots, respectively. The vector $\mathbf{a}_{SRP}$ represents the solar radiation pressure acceleration, which will be expanded and explained in more detail in Sec. V.B. Vectors $\mathbf{r}_{13}$ and $\mathbf{r}_{23}$, represented in Fig. 3, denote the position of the sunshade in the SRF with respect to the Sun and Earth, respectively, and are defined as:

$$\mathbf{r}_{13} = [x + \mu \quad y \quad z]^T \tag{3a}$$

$$\mathbf{r}_{23} = [x - (1-\mu) \quad y \quad z]^T \tag{3b}$$

To further simplify the equations of motion (EOM), it is convenient to introduce the potential U [37]:

$$U = -\frac{1}{2}\left(x^2 + y^2\right) - \left(\frac{1-\mu}{r_{13}} + \frac{\mu}{r_{23}}\right) \tag{4}$$

so that the equation of motion (EOM) becomes:

$$\ddot{\mathbf{r}} = -2\boldsymbol{\omega} \times \dot{\mathbf{r}} - \nabla U + \mathbf{a}_{SRP} \tag{5}$$

B. Solar Radiation Pressure Acceleration

As mentioned in Sec. V.A, for a large sunshade the solar radiation pressure acceleration should be accounted for. Indeed, especially in the vicinity of an equilibrium point, the magnitude of the solar radiation pressure acceleration is comparable to the gravitational accelerations exerted by the primaries [39]. Moreover, by changing the orientation of the sunshade, the acceleration vector can be controlled, similar to a solar sail [35]. The main advantage of exploiting solar radiation pressure to control the motion of the sunshade is that no propellant is required.

In this work, an ideal sail model is used to model the sunshade. An ideal sunshade reflects all photons in a specular manner; in other words, diffuse reflection, absorption, and emission are neglected. This type of sunshade is similar to an ideal mirror, whose performance could in theory be achieved by a sunshade constituted by a perfectly smooth membrane without wrinkles. Losses due to absorption, re-emission, and non-specular reflection are generally small compared to the magnitude of the reflective part: for realistic sunshades, approximately 94% of the incident radiation is reflected in the specular direction, with absorption coefficients as low as 0.04 [35]. Therefore, considering an ideal sunshade is

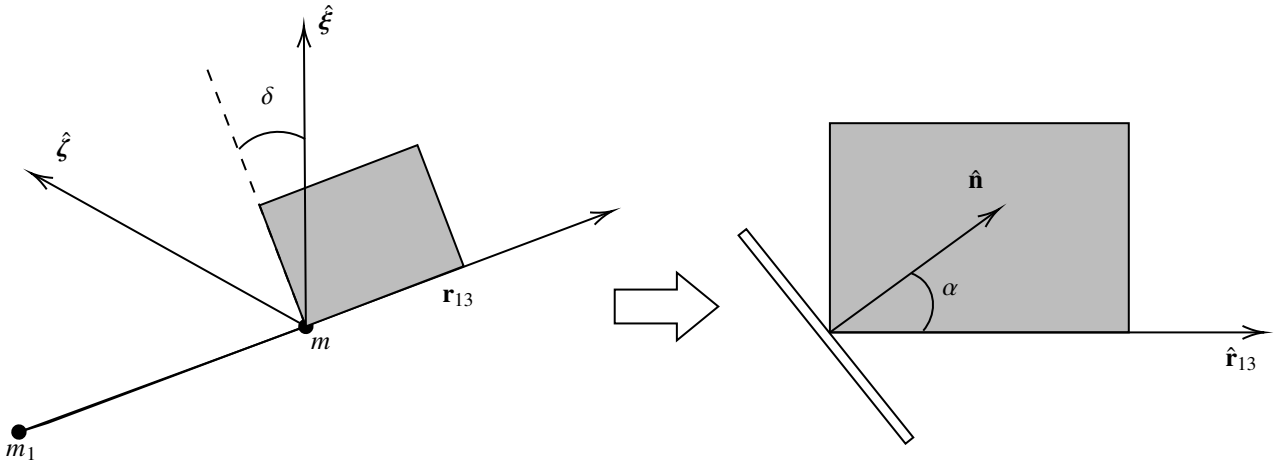

Fig. 4 Representation of the Local Reference Frame (LRF), L($\hat{\mathbf{r}}_{13}$, $\hat{\boldsymbol{\zeta}}$, $\hat{\boldsymbol{\xi}}$), adapted from Reference [40].

justified in the context of this preliminary trajectory design study. The performance of an ideal sunshade with area A and mass m is uniquely characterized by the lightness number β, defined as follows:

$$\beta = \frac{mA}{\sigma} \tag{6}$$

where $\sigma = 1.53\, gm^{-2}$ is the critical solar sail loading parameter for the solar system [35]. The SRP acceleration $\mathbf{a}_{SRP}$ acting on the sunshade can be expressed as [35]:

$$\mathbf{a}_{SRP} = \beta \frac{1-\mu}{r_{13}^2} (\hat{\mathbf{r}}_{13} \cdot \hat{\mathbf{n}})^2 \hat{\mathbf{n}} \tag{7}$$

As mentioned before, the solar radiation pressure acceleration depends on the sunshade's position and orientation with respect to the Sun, quantified in the SRF through vectors $\mathbf{r}$ and $\hat{\mathbf{n}}$ (the vector normal to the surface of the sunshade), respectively.

To define the attitude angle of the sunshade, a new reference frame is introduced, the Local Reference Frame (LRF), L($\hat{\mathbf{r}}_{13}$, $\hat{\boldsymbol{\zeta}}$, $\hat{\boldsymbol{\xi}}$) [35], represented in Fig. 4. The LRF is centered at the center of mass of the sunshade, with one axis that coincides with the vector connecting the Sun and the sunshade, $\hat{\mathbf{r}}_{13}$. The second axis is defined as:

$$\hat{\boldsymbol{\zeta}} = \hat{\mathbf{z}} \times \hat{\mathbf{r}}_{13} \tag{8}$$

The third axis of the LRF, $\hat{\boldsymbol{\xi}}$, completes the right-handed reference frame. The attitude of the sunshade can be defined by two angles: the cone angle α and the clock angle δ. The cone angle is defined as the angle between the direction normal to the sail, $\hat{\mathbf{n}}$, and the Sun-sunshade vector, $\hat{\mathbf{r}}_{13}$:

$$\alpha = \cos^{-1}\left(\hat{\mathbf{r}}_{13} \cdot \hat{\mathbf{n}}\right) \tag{9}$$

The clock angle is the angle between the projection of the acceleration vector onto the $\zeta\xi$ plane and the direction represented by $\hat{\boldsymbol{\xi}}$:

$$\delta = \cos^{-1}\left\{\left[\hat{\mathbf{r}}_{13} \times (\hat{\mathbf{n}} \times \hat{\mathbf{r}}_{13})\right] \cdot \hat{\boldsymbol{\xi}}\right\} \tag{10}$$

C. Equilibrium Solutions

If the perturbing acceleration $\mathbf{a}_{SRP}$ is neglected, five classical equilibrium solutions can be found by substituting $\mathbf{r} = \dot{\mathbf{r}} = \mathbf{a}_{SRP} = \mathbf{0}$ into Eq. 5, yielding $\nabla U = \mathbf{0}$. These solutions correspond to the five Lagrangian points: three collinear points (with $x = 0$) and two equilateral points (with $x \neq 0$). For obvious reasons, the first Lagrangian point,

L_1, is an ideal location for a planetary sunshade, as it is located between the Sun and the Earth throughout the revolving motion of the Earth around the Sun, without the need of performing large orbital maneuvers.

The addition of the solar radiation pressure acceleration expands the set of five equilibrium points to an *infinite* set of equilibrium solutions (again derived from Eq. 5):

$$\nabla U = \mathbf{a}_{SRP} \tag{11}$$

From Eq. 11, it is clear that the equilibrium solutions depend on the characteristics of the sunshade through the term $\mathbf{a}_{SRP}$ [34]. These equilibrium solutions are often called *(solar sail) displaced* equilibrium points or Artificial Equilibrium Points (AEPs) and they will be useful for the remainder of this work. A representation of a set of selected equilibrium solutions for the Sun-Earth CR3BP is reported in Fig. 5. Contour lines and arrows represent the lightness number and sunshade orientation, respectively, that are required to achieve equilibrium. It can be noticed from Fig. 5 that achieving equilibrium in certain locations is not possible. This is due to the fact that the SRP acceleration can only be oriented away from the Sun. Furthermore, it is also clear from Fig. 5 that a static sunshade in the ecliptic plane must be located between the Sun and the classical L_1 point; in addition, to increase the distance from L_1 corresponds a larger lightness number is required.

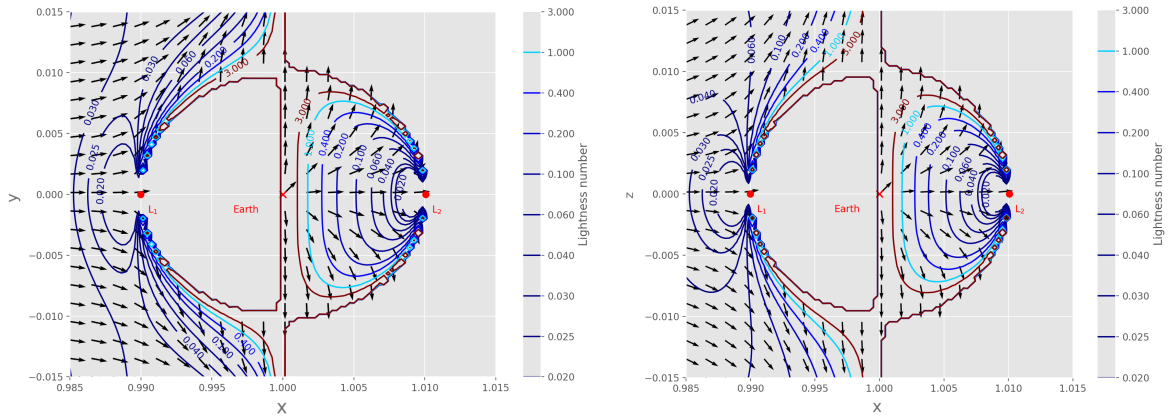

Fig. 5 Distribution of Artificial Equilibrium Points in the vicinity of the Earth, plotted in the xy-plane (left panel) and in the xz-plane (right panel). The required lightness number β is represented by countour levels, while the required sunshade orientation is indicated by black arrows.

VI. Insolation

The focus of the paper is now shifted towards the computation of the solar irradiance and of its reduction due to the sunshade. Fundamental quantities are introduced below. The spatio-temporal distribution of the natural insolation received by the Earth is presented in Sec. VI.A, while different eclipse conditions are described in Sec. VI.B. The section is concluded with the explanation of the solar limb darkening model adopted for this work (Sec. VI.C).

The irradiance, S, is defined as the power emitted or received by a unit surface [41]. The solar irradiance received by the Earth, averaged over one year, is usually referred to as the solar constant, S_0. According to the most recent satellite measurements [42], its value oscillates between 1360 and 1365 Wm^{-2}, depending on the eleven-year solar cycle. The irradiance can be converted to the radiance, I, which is defined as the radiating power emitted or received by a unit surface per unit solid angle [41]:

$$S = \Omega I \tag{12}$$

where Ω is the solid angle subtended by a generic surface. These definition will be useful for the remainder of this section.

A. Natural Insolation

Solar irradiance is a good metric to evaluate the global energy balance of the Earth. However, since it is defined as the solar flux reaching a unit surface perpendicular to the direction of solar radiation, it is not a suitable metric to evaluate its impact on the Earth's climate. A more representative quantity in this context is the insolation, Q, that adjusts the value of the solar constant for different locations on the Earth and for different times during the year. The temporal dependency is expressed through the varying Sun-Earth distance, $r_\oplus$, while the spatial dependency is quantified by the solar zenith angle, ψ, as follows [43]:

$$Q = S_0 \left(\frac{\bar{r}_\oplus}{r_\oplus} \right)^2 \cos\psi \tag{13}$$

with $\bar{r}_\oplus$ the average Sun-Earth distance (1 AU). The solar zenith angle, ψ, is defined as the angle between the normal to the Earth's surface at a given point P and the direction in which solar radiation reaches at the same point [43]. The solar zenith angle depends on the latitude, on the season, and on the time of day as follows [43]:

$$\cos\psi = \sin\lambda \sin\nu + \cos\lambda \cos\nu \cos h \tag{14}$$

All quantities from Eq. 14 are depicted in Fig. 6. The latitudinal dependence is expressed through the latitude angle λ, while the seasonal dependence is expressed via the declination angle ν, which is the latitude of the point on the Earth's surface where the Sun is at zenith at noon. The time of the day is expressed via the hour angle, which is the longitude of point P during the day, expressed with respect to its position at noon [43]. Equation 14 holds everywhere on Earth, except at the poles: in the summer hemisphere, latitudes higher than $\lambda = 90^\circ - \nu$ are in constant daylight, while in the winter hemisphere such locations are not reached by sunlight at all.

It is possible to find the daily average of Eq. 13, $\overline{Q}$, by computing the integral over all hour angles between $-h_0$ (hour angle at sunrise) and $+h_0$ (hour angle at sunset) [43]:

$$\overline{Q} = \frac{S_0}{\pi} \left(\frac{\bar{r}_\oplus}{r_\oplus} \right)^2 (h_0 \sin\lambda \sin\nu + \cos\lambda \cos\nu \cos h_0) \tag{15}$$

The insolation distribution resulting from Eq. 15 is reported in Fig. 7. The contour lines denote the insolation level, while the dashed line shows the latitude of the subsolar point at local noon. It can be noticed that the poles do not receive any insolation (constant darkness) during local winter; on the other hand, during local summer, they receive the greatest amount of insolation, due to the tilt of the Earth's spinning axis. Finally, the latitude of the subsolar point at local noon (dashed line) oscillates between the latitude of the tropic of Cancer (reached on the summer solstice) and the tropic of Capricorn (reached on the winter solstice).

B. Radiance reduction under eclipse conditions

The attention is now shifted towards the computation of the radiance reduction due to the shade. In the presence of a radiating body (usually the Sun) and a shading body, four different eclipse regions arise: the fully illuminated region, the *umbra* region (total eclipse), the *penumbra* region, and the annular eclipse region. These regions are represented in Fig. 8 and are denoted as follows:

$$I = \begin{cases} I_0 & \text{fully illuminated} \\ I_{\text{pe}} & \text{partial eclipse} \\ I_{\text{ae}} & \text{annular eclipse} \\ 0 & \text{total eclipse} \end{cases} \tag{16}$$

with $0 < I_{\text{pe}} < I_0$ and $0 < I_{\text{ae}} < I_0$. Most methods available in literature to compute the eclipse condition of an orbiting body are derived for satellites in Low Earth Orbit (LEO), therefore the main objective of these methods is to determine whether a spacecraft is in total eclipse or, alternatively, fully exposed to sunlight, but nothing in between (see References [45, 46]). These methods are therefore not suitable for the purpose of this work, where the radiance reduction due to partial or annular eclipses has to be determined. As a result, the method described in Reference [47] is adopted. The radiating body (the Sun) is assumed to be perfectly spherical and the radius of its projected disk is denoted by $R_\odot$; the planetary sunshade is assumed to be perfectly circular and its radius is denoted by R_D. The Sun and the sunshade are centered at points S and D, respectively, as indicated in Fig. 8. The sufficient conditions for each eclipse region are reported in [47]. To quantify the insolation reduction due to the shade, vectors $\mathbf{r}_{\odot,P}$ and $\mathbf{r}_{D,P}$ are introduced, denoting

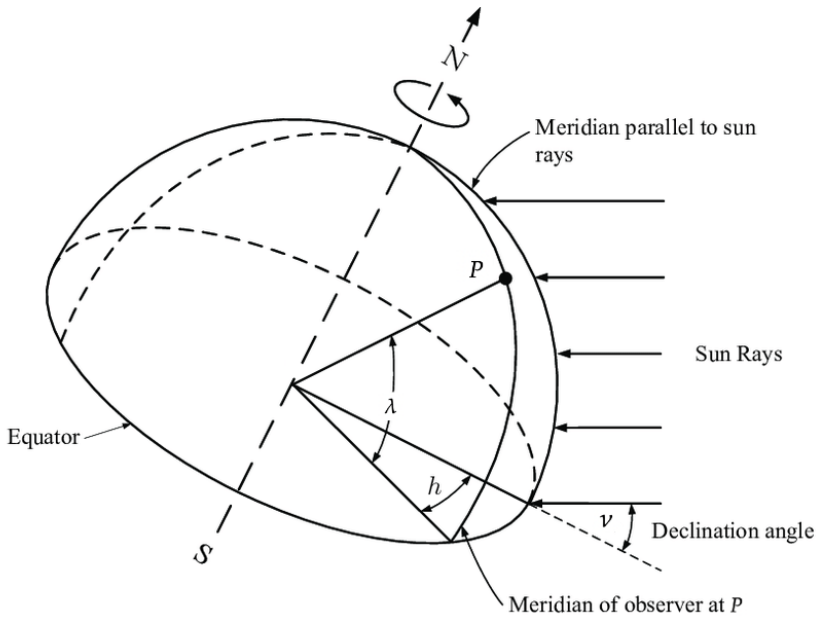

Fig. 6 Representation of the latitude angle, λ, the declination angle, ν, and the hour angle, h (adopted from Reference [44]).

the position of the Sun and the sunshade with respect to a generic point P on the Earth's surface, respectively. Solid angles $\Omega_\odot$ and Ω_D, quantifying the angular radius of the Sun and the sunshade respectively, are also introduced:

$$\Omega_\odot = \sin^{-1}\left(\frac{R_\odot}{r_{\odot,P}}\right) \tag{17}$$

$$\Omega_D = \sin^{-1}\left(\frac{R_D}{r_{D,P}}\right) \tag{18}$$

The parameter η, denoting the angular separation between the Sun and the sunshade, is defined as [47]:

$$\eta = \cos^{-1}\left(\frac{\mathbf{r}_{\odot,P}\cdot\mathbf{r}_{D,P}}{r_{\odot,P}\cdot r_{D,P}}\right) \tag{19}$$

The radiance under partial eclipse condition, I_{pe}, can then be computed as follows [47]:

$$\begin{aligned} I_{\text{pe}} =& I_0\left\{1-\frac{1}{\pi\left(1-\cos\Omega_\odot\right)}\left[\pi-\cos\Omega_\odot\cos^{-1}\left(\frac{\cos\Omega_D-\cos\Omega_\odot\cos\eta}{\sin\Omega_\odot\sin\eta}\right)+\right.\right. \\ &\left.\left.-\cos\Omega_D\cos^{-1}\left(\frac{\cos\Omega_\odot-\cos\Omega_D\cos\eta}{\sin\Omega_D\sin\eta}\right)-\cos^{-1}\left(\frac{\cos\eta-\cos\Omega_\odot\cos\Omega_D}{\sin\Omega_\odot\sin\Omega_D}\right)\right]\right\} \end{aligned} \tag{20}$$

while the radiance in annular eclipse, I_{ae}, can be computed as follows [47]:

$$I_{\text{ae}} = I_0\left(1-\frac{1-\cos\Omega_D}{1-\cos\Omega_\odot}\right) \tag{21}$$

Given the geometry of the Sun–sunshade–Earth system under the assumptions presented in Sec. IV, the Earth's surface is never in total eclipse, but it oscillates between annular eclipse and partial eclipse, depending on the relative position of the sunshade.

C. Solar Limb Darkening

Equations 20 and 21 are based on the assumption that the illuminating body radiates homogeneously. However, this assumption is not justified when a planetary sunshade is present. Indeed, the apparent solar luminosity is larger at the

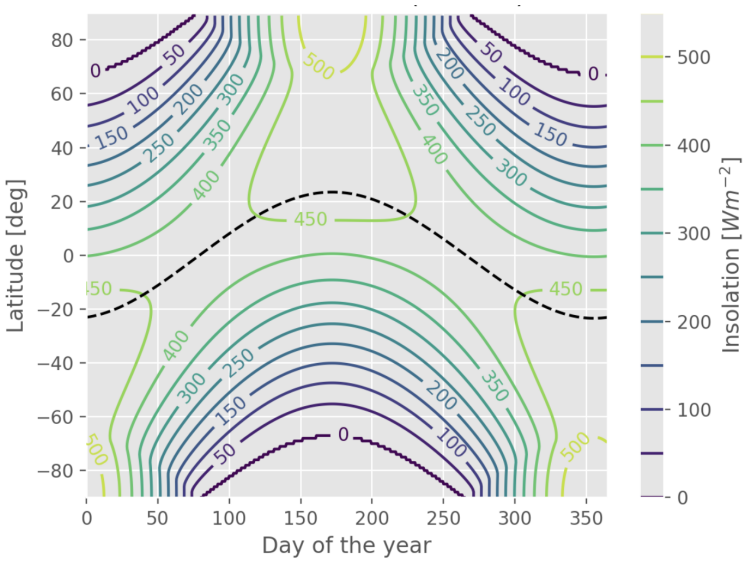

Fig. 7 Insolation received by the Earth in nominal conditions over one year ($S_0 = 1360\,Wm^{-2}$). Countour levels indicate the insolation, while the dashed line denotes the latitude of the subsolar point at local noon.

center of the solar disk and smaller at its outer edges [48]. The radial dependency of the apparent solar luminosity, known in literature as *limb darkening*, has the direct implication that the same sunshade shading different regions of the solar disk results in different radiance distributions on the Earth's surface. Most limb darkening models available in literature are empirical and are based on polynomial interpolations of solar observations (e.g., [49]). In this work, the second-degree polynomial approximation proposed in Reference [50] (computed for a mean wavelength of 550 nm) is adopted. The geometry of the model is described in Fig. 9. The limb darkening can then be computed as follows [50]:

$$I_r = I_c \left(c_0 + c_1 \cos\gamma + c_2 \cos^2\gamma\right) \tag{22}$$

where I_c is the radiance emitted by the center of the Sun and I_r is the radiance emitted by the Sun at a radial distance d_r from its center. c_0, c_1, and c_2 are empirical coefficients and their values are assumed from Reference [50] ($c_0 = 0.3$, $c_1 = 0.93$, and $c_2 = -0.23$). With this set of coefficients, it is assumed that the brightness of the Sun at its limb is equal to 30% of the brightness at its center. The radial distance, d_r, is related to the angle γ as follows:

$$\frac{d_r}{R_\odot} = \sin\gamma \tag{23}$$

As a result, the radiance seen by an observer in fully illuminated conditions, I_0, results in:

$$I_0 = \int_0^{R_\odot} I_r(d_r)\,\mathrm{d}\,d_r \tag{24}$$

where the integral spans the entire radial extension of the Sun. In this paper, Eq. 24 is discretized over ten different values of the radial distance to reduce the computational effort. A representation of this approximation is reported in Fig. 10. The ten values are discretized in the range $0 < \frac{I_r}{I_c} < 1$ so that the radiance emitted by a solar ring between two adjacent nodes of radial distance is the same for all pairs of radial distances. This is an improvement in accuracy with respect to the method used in Reference [33], where the discretization was based on regularly spaced values of the radius of solar disks.

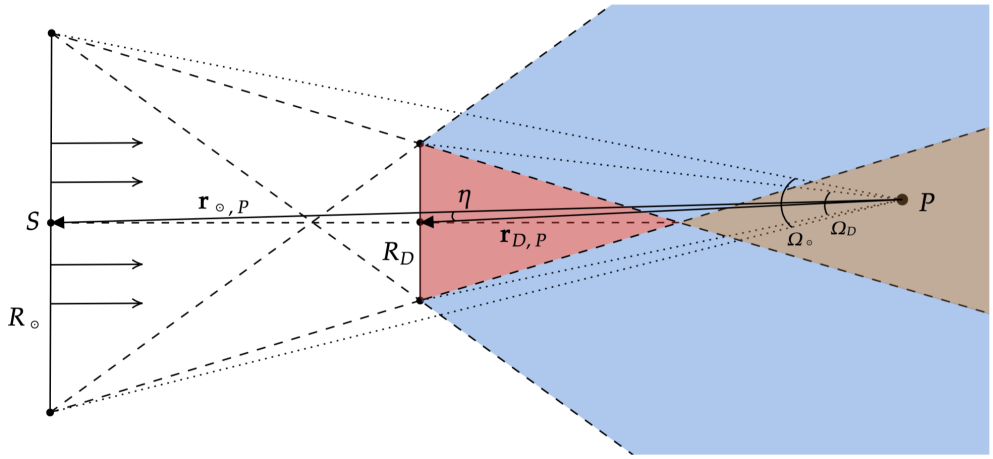

Fig. 8 Different eclipse conditions produced by a planetary sunshade of radius R_D located at a distance $|\mathbf{r}_{\odot,P} - \mathbf{r}_{D,P}|$ from the Sun: fully illuminated (white), partial eclipse (blue), annular eclipse (brown), and total eclipse (red). Solid angles $\Omega_\odot$ and Ω_D, subtended by the Sun and the sunshade at point P, respectively, are also represented.

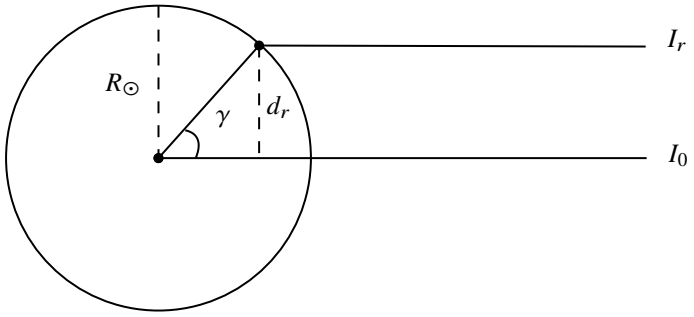

Fig. 9 Geometry of solar limb darkening: the radiance emitted by the Sun decreases with increasing radial distance d_r.

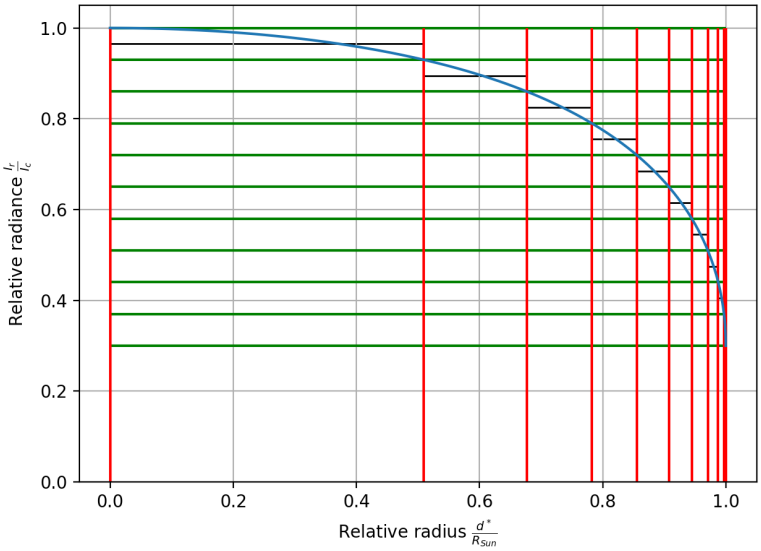

Fig. 10 Discretization of solar limb darkening: empirical law representing Eq. 22 (blue), ten equidistant levels of relative radiance (green), and resulting discrete levels for the relative radius (red).

VII. Quantification of Climate Changes

The effect of the reduced insolation due to the sunshade produces an effect on the Earth's climate. Since the climate is a complex system, it is difficult to optimize the resulting latitudinal and seasonal insolation distribution without any data related to the climate itself [51]. Therefore, in this work a climate model is used to quantify the impact of the sunshade. Climate models are usually grouped into three classes of increasing complexity: Energy Balance Models (EBMs, [52]), Earth Models of Intermediate Complexity (EMICs, [53]), and Global Circulation Models (GCMs, [54]). Although EMICs and GCMs accurately reproduce most climate features, they are very computationally expensive and not suitable to be run within an optimization loop. Therefore, a specific EBM, the Globally Resolved Energy Balance (GREB) model, is adopted [36]. The choice is motivated by two factors. Firstly, GREB is the only globally resolved EBM available in literature. Thus, it is possible to supply the model with a latitude-dependent insolation distribution, rather than a single value, like it would be when considering a uniform reduction in the solar constant [55]. Secondly, GREB was used in the work in Reference [33], which enables cross-validation and comparison of the results.

GREB is based on a simplified energy balance and accounts for several sources of heat flux, F: the heat flux from shortwave (solar), F_{solar}, and longwave (thermal) radiation, F_{thermal}, the heat exchanged within the atmospheric hydrological cycle, F_{latent}, the heat flux exchanged with the deep oceans, F_{ocean}, and the sensible heat flux, F_{sense}. Heat transfer via atmospheric circulation (advection and diffusion) is also accounted for. Such processes are modeled in a simplified way that prioritizes computational efficiency over accuracy. It features three different layers (a single-slab atmosphere, surface land, and a single-layer deep ocean) resolved on a grid of 3.75° x 3.75° in latitude (angle λ) and longitude (angle φ). The grid's spatial resolution corresponds to roughly 400 km, which is comparable to the resolution of several GCMs [54]. The temperature at each node of these three layers (atmosphere, land surface, and ocean) represent GREB's main prognostic variables [36]: $T_{\text{atm}}(\lambda, \varphi, t)$, $T(\lambda, \varphi, t)$, $T_{\text{ocean}}(\lambda, \varphi, t)$, where t denotes the time dependency. The land surface energy balance is described by the following equation (it is noted that energy balance equations for the atmosphere and the deep ocean have similar forms, therefore they are not reported here):

$$\tau_{\text{surf}} \frac{\mathrm{d}T}{\mathrm{d}t} = F_{\text{solar}} + F_{\text{thermal}} + F_{\text{latent}} + F_{\text{ocean}} + F_{\text{sense}} + F_{\text{correct}} \tag{25}$$

where T is the surface temperature and τ_{surf} its heat capacity. The term F_{correct} represents empirical corrections: indeed, for most EBMs and EMICs, models are adjusted with empirical values to correct for deviations due to model biases [36]. This correction is achieved by performing a shorter climate simulation that computes the heat fluxes needed to maintain the prognostic variables equal to their observed counterparts. It is of interest for this work to expand the forcing term quantifying the shortwave radiative energy flux, F_{solar} , as follows:

$$F_{\text{solar}} = (1 - \chi_{\text{clouds}})(1 - \chi_{\text{surf}})\, Q \tag{26}$$

where Q is the insolation introduced in Eq. 15, while χ_{clouds} and χ_{surf} are the cloud and surface albedo, respectively. Introducing a planetary sunshade affects the insolation Q and its temporal and latitudinal distribution, which in turn plays a role in the surface temperature via the GREB model equations. The GREB model needs a set of historical average climatologies as input data, both to estimate the empirical corrections (surface temperature, atmospheric temperature, and deep ocean temperature) and to provide the model with boundary conditions (horizontal winds, CO_2 levels, topographic height, surface wetness, ocean mixed layer depth, and cloud cover). While GREB is unable to reproduce small-scale and short-term climate variability (i.e., weather fluctuations), it is a reasonably accurate and particularly fast tool to evaluate global trends in climate change due to modifications in the external forcings [33, 36, 55]. Simulating 50 years of climate evolution takes approximately 10 minutes on a standard Personal Computer (PC), as reported also in Reference [33]. However, caution should be exerted, since GREB — like all EBMs — does not include *all* types of climate feedback. It is therefore unable to reproduce small-scale climate changes that could be of great importance when it comes to evaluating the impact of a geoengineering scheme. The authors of the models claim that its uncertainties are comparable to the models used by the International Panel on Climate Change (IPCC) [36]. Still, more accurate models should be used when a more precise assessment of solar geoengineering schemes are needed. GREB was originally written in Fortran and its source code, together with the required input data, are freely available through [36]. For the purpose of this work, the source code was converted into Python code; the input data were taken from [36].

In the remainder of this work, four different climate simulations are performed with GREB. The first climate simulation (case A), denoted by the subscript $\square_{\text{ref}}$, is a reference scenario with pre-industrial levels of atmospheric CO_2 content (see Table 1) and the natural insolation distribution. The second climate simulation (case B), denoted by the subscript $\square_{\text{2xCO2}}$ is the same as case A, but with doubled amount of atmospheric CO_2 content (680ppm). The third and

Table 2 Climate scenarios considered.

Case	Name	Notation	CO_2 [ppm]	Sunshade
A	Reference	$\square_{\text{ref}}$	340	Absent
B	2xCO2	$\square_{\text{2xCO2}}$	680	Absent
C	Geoengineering - static	$\square_{\text{geo}}^{\text{static}}$	680	Static
D	Geoengineering - dynamic	$\square_{\text{geo}}^{\text{dynamic}}$	680	Dynamic

fourth climate simulations (case C and D), denoted by the subscript $\square_{\text{geo}}$, are the same as case B, but with an artificial insolation distribution, with the latter varying according to the sunshade trajectory and configuration. All the scenarios considered in this work are summarized in Table 2.

VIII. Numerical optimization

In this section, the numerical optimization techniques used in this work are described. The optimal control problem to find a time-optimal transfer trajectory connecting two given artificial equilibrium points is introduced in Sec. VIII.A. The optimal control problem constitutes the "inner" loop of the pipeline described in Fig. 2 (i.e., it is part the "transfer trajectory optimization" process in Fig. 2). Furthermore, the heuristic optimization problem and the associated genetic algorithm used are described in Sec. VIII.B. The heuristic optimization constitutes the "outer" loop of the pipeline described in Fig. 2.

A. Transfer Trajectory Optimization

As anticipated in Sec. IV, the transfer trajectory between artificial equilibrium points is found by solving an optimal control problem [56, 57]. In this work, a direct method based on collocation is used. Direct methods convert (or *transcribe*) an optimal control problem into a finite non-linear programming (NLP) problem. This is achieved by dividing the trajectory into segments through a mesh of nodes (spaced, for example, in time). Across each segment, the state and control variables are approximated by means of polynomial interpolation. In this work, both the state and control variables are discretized on the time domain using Lagrange-Radau polynomials [58]. At the boundaries of the segment, the polynomial must satisfy the dynamical constraints. In addition, at one or more points within the segment (called *collocation* points), the interpolated derivatives are compared to the derivatives computed through the EOM. The difference, called *defect*, is minimized by the solver [56]. Considering all segments of the trajectory, a set of algebraic equations expressed in terms of the state and control variables emerges.

In this work, the state variables $\mathbf{X}_1(t)$ are the position and velocity components of the sunshade in the SRF:

$$\mathbf{X}_1(t) = [x \quad y \quad z \quad \dot{x} \quad \dot{y} \quad \dot{z}]^T \tag{27}$$

The control variables $\mathbf{U}(t)$ are the components of the vector normal to the sail, introduced in Sec. V.B, expressed in the SRF:

$$\mathbf{U}(t) = \hat{\mathbf{n}} = [n_x \quad n_y \quad n_z]^T \tag{28}$$

The objective function J_1 to be minimized is the time of flight:

$$J_1 = t_f - t_i \tag{29}$$

where t_i and t_f are the times corresponding to the start and end of the transfer trajectory, respectively.

Several constraints are imposed. Dynamic constraints, represented by the equation of motions (Eq. 5), are imposed. Additionally, two path constraints are formulated. The first path constraint ensures that the norm of the control vector equals unity:

$$|\mathbf{n}| = 1 \tag{30}$$

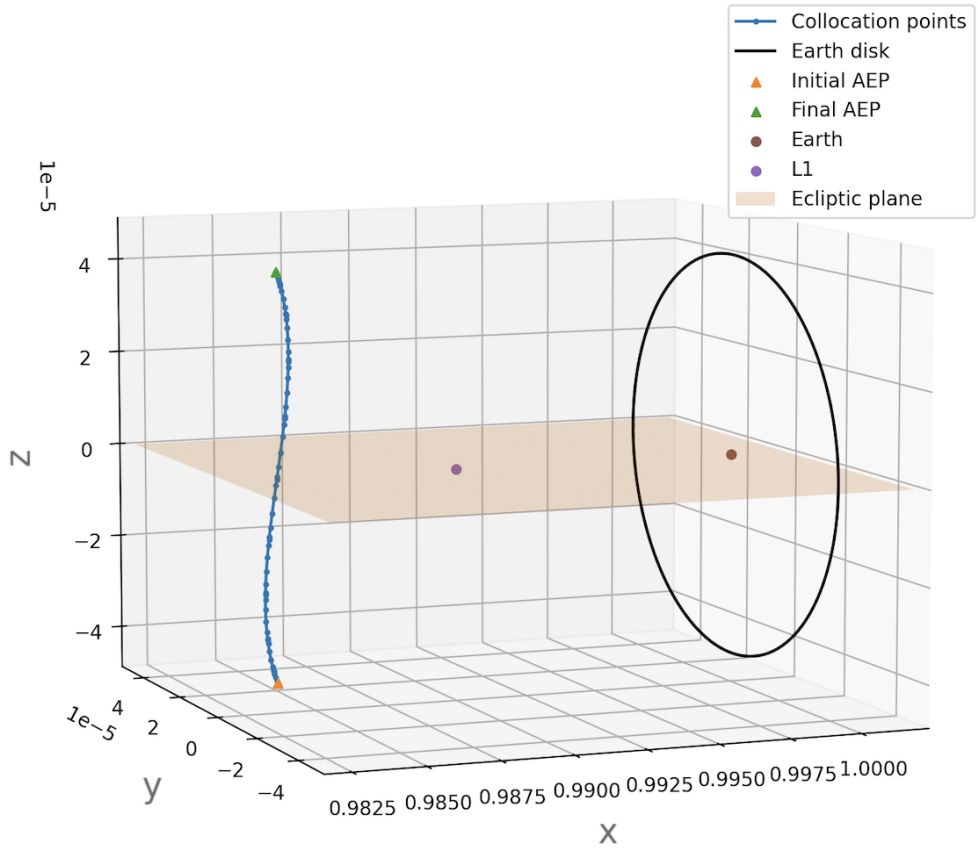

Fig. 11 Time-optimal transfer trajectory originating from $z = -R_\oplus$ and ending at $z = +R_\oplus$. It is noted that the z-axis is stretched with respect to the x- and y-axes.

The second path constraint ensures that the SRP acceleration vector points away from the Sun [35]:

$$\mathbf{r}_{13} \cdot \hat{\mathbf{n}} \geqslant 0 \tag{31}$$

Boundary conditions are also imposed on the initial and final state and control variables:

$$\mathbf{X}_1(t_i) = \mathbf{X}_i \tag{32a}$$
$$\mathbf{X}_1(t_f) = \mathbf{X}_f \tag{32b}$$
$$\mathbf{U}(t_i) = \mathbf{U}_i \tag{32c}$$
$$\mathbf{U}(t_f) = \mathbf{U}_f \tag{32d}$$

The first two equations ensure that the transfer trajectory of the sunshade begins and ends at given AEPs, while the last two equations ensure that equilibrium is satisfied at the start and end locations. In this work, the problem was discretized by dividing the time of flight, $t_f - t_i$, in ten segments. Each segment was composed of six collocation points. For some trajectories, variations of these settings have been performed in order for the problem to converge. For all the other settings, default values are used. An open-source, Python-based optimization modeling package, called `Pyomo`, is used [59]. Pyomo relies on the Interior Point Optimizer (IPOPT), an open-source package for large-scale optimization [60]. Pyomo allows users to model the optimization problem and use direct methods to transcribe a dynamic optimization problem into a large-scale, sparse, static optimization problem through collocation methods. The NLP problem is then solved by IPOPT.

An example of a transfer trajectory between two AEPs is reported in Fig. 11, while the attitude angles required to achieve such a trajectory are plotted in Fig. 12. The transfer starts at $z = -R_\oplus$ and ends at $z = +R_\oplus$, taking approximately 56 days. It is possible to notice how the trajectory and the cone angle profile are rather symmetric with

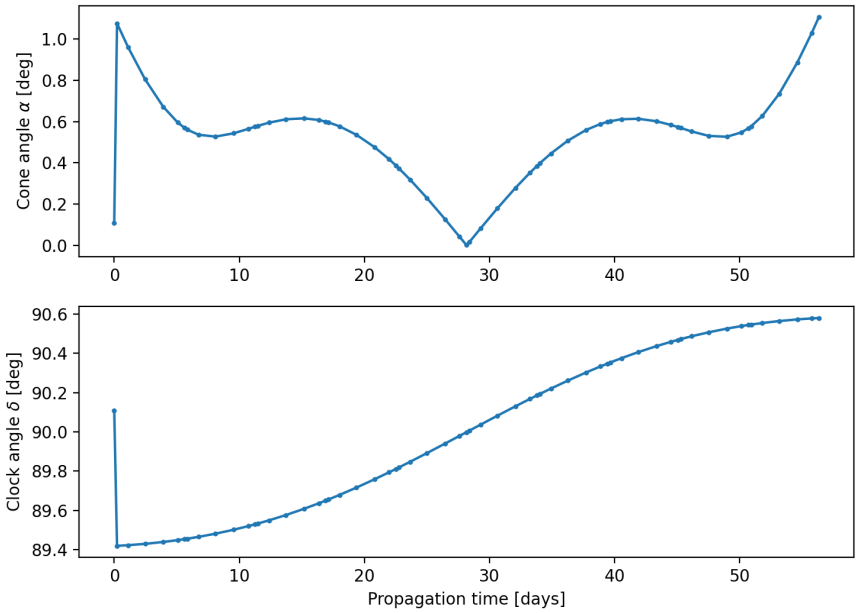

Fig. 12 Attitude angles required to achieve the transfer trajectory presented in Fig. 11. Top panel: cone angle, α; bottom panel: clock angle, δ.

respect to the midpoint of the transfer. These features are directly related to the fact that the ecliptic plane is a plane of symmetry for the CR3BP. Furthermore, given the relatively small distance travelled by the sunshade, the attitude angle shows small variations, in the order of 1°. Given that the objective is to minimize the transfer time, the trajectory results in a nearly-straight, elongated transfer, with a very large variation in the z-coordinate and small variations for the x- and y-coordinates.

B. Minimization of Temperature Anomalies

As stated in Sec. IV, the goal of this work is to optimize the location of the sunshade over a full year to minimize latitudinal temperature anomalies. For this purpose, three different problems are defined, each with a different objective, and then solved via a genetic algorithm. This process corresponds to the "outer" loop reported in Fig. 2. However, before doing so, the design space is explored through grid searches that analyze the relation between the independent variables and two of the three objective functions. All the optimization problems explained below are unconstrained and single-objective.

The objectives used for the optimization are threefold. The first two objectives are also used as dependent variables in the grid searches. First, an objective function J_{RMS} that quantifies the latitudinal distribution of temperature anomalies is considered, as suggested by Reference [33]. The GREB model produces monthly means of surface temperature data for each node of the spatial grid. This is denoted as $\bar{T}(\lambda, \varphi, i)$, with index $i = 0, 1, \ldots, 11$ referring to the month of the year; as presented in Sec. VI, the latitudinal and longitudinal dependencies are respectively denoted by the latitude angle λ and the longitude angle φ. The overbar indicates that this quantity is a monthly average. The spatial grid is discretized through 96 points over the longitude and 48 points over the latitude, resulting in 4608 nodes and a spatial resolution of 3.75° (corresponding to roughly 400 km, as stated in Sec. VII). For such a grid, the longitudinally averaged temperature is:

$$\bar{T}(\lambda, i) = \frac{1}{96} \sum_{\varphi=0^\circ}^{360^\circ} \bar{T}(\lambda, \varphi, i) \tag{33}$$

From Eq. 33, the temperature anomaly is computed by taking the difference between the double-CO_2 geoengineering

scenario (subscript $\square_{\text{geo}}$) and the reference scenario (subscript $\square_{\text{ref}}$):

$$\Delta\bar{T}(\lambda,i) = \bar{T}_{\text{geo}}(\lambda,i) - \bar{T}_{\text{ref}}(\lambda,i) \tag{34}$$

Then, the root mean squares (RMS) is used to account for both negative and positive temperature anomalies over time:

$$\Delta\bar{T}(\lambda) = \sqrt{\frac{1}{12}\sum_{i=0}^{11}\Delta\bar{T}^2(\lambda,i)} \tag{35}$$

Finally, the resulting values are averaged over latitude weighted for the surface area corresponding to each latitudinal grid point. The surface area for each grid point, $\Delta A(\lambda,\varphi)$, can be computed as [61]:

$$\Delta A(\lambda,\varphi) = R_{\oplus}^2\,\Delta\lambda\,\Delta\varphi\cos\lambda \tag{36}$$

Equation 36 represents both the case where the Earth radius is latitude-dependent (ellipsoidal Earth model) or constant (spherical Earth model). In this work, a spherical Earth model is used; therefore, for a regularly spaced grid as the one used in this work, the surface area $\Delta A(\lambda)$ is only latitude-dependent. The objective function sought for can then be defined as:

$$J_{\text{RMS}} = \sum_{\lambda=-90^\circ}^{90^\circ}\Delta A(\lambda)\Delta\bar{T}(\lambda) \tag{37}$$

It should be noted that the objective function J_{RMS} is only computed over the last year of the simulation (50^{th} year). It is also possible to include a filter after Eq. 35, so that only statistically relevant temperature anomalies are accounted for. This method was proposed in Reference [33], using a threshold of statistical relevance of 0.1°C.

The second objective function, J_{GMST}, quantifies the global temperature anomaly, without accounting for regional or latitudinal differences. The surface temperature is averaged by longitude, by latitude, and by month of the year, to obtain the Global Mean Surface Temperature (GMST), denoted by $\bar{T}^{\text{global}}$:

$$\bar{T}^{\text{global}} = \frac{1}{96}\frac{1}{48}\frac{1}{12}\sum_{\varphi=0^\circ}^{360^\circ}\sum_{\lambda=-90^\circ}^{90^\circ}\sum_{i=0}^{11}\bar{T}(\lambda,\varphi,i) \tag{38}$$

Subsequently, the global mean surface temperature, $\bar{T}^{\text{global}}$, is used to compute the temperature anomaly:

$$J_{\text{GMST}} = \bar{T}_{\text{geo}}^{\text{global}} - \bar{T}_{\text{ref}}^{\text{global}} \tag{39}$$

In this case, it is also possible to introduce a filtering scheme to discard statistically insignificant values.

Finally, it is also useful to introduce a third objective function, J_{polar}, that quantifies the Polar Mean Surface Temperature (PMST) anomaly. This is essentially a variation of the objective function J_{GMST}, computed only over the polar regions. In this work, polar regions are defined as regions with latitude $|\lambda| > 67.5^\circ$. Therefore, Eq. 38 can be transformed into:

$$\bar{T}^{\text{polar}} = \frac{1}{96}\frac{1}{12}\frac{1}{12}\sum_{\varphi=0^\circ}^{360^\circ}\sum_{i=0}^{11}\left(\sum_{\lambda=-90^\circ}^{-67.5^\circ}\bar{T}(\lambda,\varphi,i) + \sum_{\lambda=67.5^\circ}^{90^\circ}\bar{T}(\lambda,\varphi,i)\right) \tag{40}$$

yielding:

$$J_{\text{polar}} = \bar{T}_{\text{geo}}^{\text{polar}} - \bar{T}_{\text{ref}}^{\text{polar}} \tag{41}$$

The objective function formulated in Eq. 41 is useful to evaluate the sunshade's performance over the poles, which are sensitive regions for climate change showing the largest surface temperature increase.

The independent variables of all optimization problems are the following, grouped in the decision vector $\mathbf{X}_2$:

$$\mathbf{X}_2 = \begin{bmatrix} z_S & z_N & t_S & t_N \end{bmatrix}^T \tag{42}$$

Quantities z_S and z_N denote respectively the vertical displacement of the AEPs below (subscript $\square_S$) and above (subscript $\square_N$) the ecliptic plane. As presented in Sec. IV, the x- and y-coordinates of the AEPs are fixed and their values are reported in Table 1, therefore only the z-coordinate is optimized. As a result, the optimal AEP found will not be a true equilibrium point. Analogously, t_S and t_N denote the time when the transfer from south to north and from north to south

start, respectively. Both t_S and t_N are measured in days from January 1st. Such a choice entails that the south-to-north trajectory of the sunshade is the north-to-south trajectory, yet flown backwards.

A Differential Evolution (DE) algorithm was selected to solve each of the three optimization problems [62]. In all cases, a population of 20 individuals was initialized randomly, which evolved over 20 generations. Given the computational resources required to run the GREB model for 50 years, this setup results in roughly 66 hours of runtime to solve each optimization problem using a single seed to initialize the population. To solve the optimization problems, the open-source, Python-based heuristic optimization package `PyGMO` was used in this paper [63]. The results are presented and discussed in Sec. IX.

IX. Results and discussion

In this section, the results are presented and discussed. In Sec. IX.A, the performance of a static shade is analyzed. Then, the design space for a dynamic shade is explored through grid searches in Sec. IX.B. Finally, the optimal solutions found for each objective function are presented in Sec. IX.C.

A. Static shade

In Sec. III, it was stated that a static sunshade has the disadvantage of undercooling polar regions and overcooling tropical regions. This scenario is reproduced here by modeling a static sunshade with its location and size equal to the values reported in Table 1. The results of a 50-year simulation with the GREB model accounting for the effect of the static sunshade are reported in Fig. 13. It is possible to notice negative temperature anomalies, with peaks of $-0.4\,^{\circ}$C between the +20° and -20° latitudinal bands; on the other hand, temperature anomalies over the polar regions are evidently positive. These results confirm the findings reported in literature.

Furthermore, there is a clear latitudinal asymmetry: over Antarctica, temperature anomalies are lower than $1.0\,^{\circ}$C everywhere; on the other hand, in the northern hemisphere, the same level of anomaly is already reached in the latitudinal band between +50° and +80°. At latitudes higher than +80°, the temperature anomaly is always greater than $1.0\,^{\circ}$C, with peaks of $1.4\,^{\circ}$C over North-East Asia. The gradient in temperature anomalies is larger at mid-latitudes between 45° and 70° in both hemispheres. Such an asymmetry is likely due to the different split between land and oceans: in the southern hemisphere, the ratio between land and ocean is 1 to 4, which reduced to 1 to 1.5 in the northern hemisphere [64]. In other words, the fraction of land over the total area is 20% for the southern hemisphere and 40% for the northern hemisphere. As a result, given that water has a greater heat storage capacity than land, an equal increase in radiative forcing results in a lower average surface temperature in the southern hemisphere. This pattern is even more visible if the sunshade is not present (see Fig. 1). Therefore, it is expected that the outcome of the optimization problem will reflect this difference. In terms of sunshade trajectory, this roughly means that the sunshade should spend more time over the northern hemisphere.

From a global perspective, the reference scenario (CO_2 content of 340 ppm, corresponding to pre-industrial levels, without sunshade) results in a GMST of $\bar{T}_{\text{ref}}^{\text{global}} = 13.92\ ^{\circ}$C; on the other hand, the geoengineered scenario with a static sunshade produces a GMST of $\bar{T}_{\text{geo}}^{\text{global}} = 14.15\ ^{\circ}$C, simulated with GREB. This yields a global temperature anomaly of $J_{\text{GMST}} = 0.23\ ^{\circ}$C. As explained in Sec. IV, the size and location of the sunshade are assumed from literature so that an average reduction of 1.7% in insolation is achieved. It is clear that, under the assumptions made in this work, a slightly larger reduction in insolation would be required to completely offset the global temperature anomaly, which could be achieved by a larger sunshade. As long as the assumptions made to model the sunshade do not change, the fact that the GMST anomaly is not exactly zero is not an issue for this work, since the goal is to compare different trajectory solutions and understand their effects on the climate, rather than to accurately size the sunshade.

B. Grid search

Before solving the overarching optimization problem with the heuristic algorithm (see Fig. 2), the design space is explored by means of grid searches. The goal of using a grid search method is to better understand the search space and the impact of each variable of the decision vector $\mathbf{X}_2$, defined in Eq. 42. In particular, a regular grid of points is used for both types of independent variables (z-displacement and time of departure). The z-displacement is discretized through

ten equidistant points as follows:

$$z_S^* = \frac{z}{R_\oplus} = -\frac{i}{10} \qquad \text{for } i = 1, 2, \ldots, 10 \tag{43}$$

$$z_N^* = \frac{z}{R_\oplus} = +\frac{i}{10} \qquad \text{for } i = 1, 2, \ldots, 10 \tag{44}$$

where for simplicity the z-displacement is expressed as a fraction of the Earth's radius, $R_\oplus$. This notation will be used throughout the remainder of the paper. The start dates of the transfers (t_S and t_N) are also discretized with ten equidistant points as follows:

$$t_S = 30 + 10\,i \qquad \text{for } i = 1, 2, \ldots, 10 \tag{45}$$

$$t_N = 210 + 10\,i \qquad \text{for } i = 1, 2, \ldots, 10 \tag{46}$$

where t_S and t_N are measured in days from January 1st.

Two different types of grid searches are carried out. The first grid search fixes the start dates of the transfers ($t_S = 60$ days, $t_N = 240$ days) to create a catalog of trajectories with different combinations of z-displacement

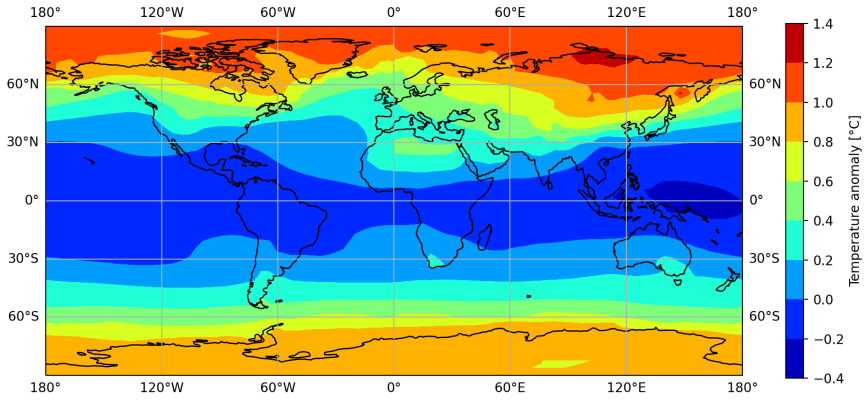

Fig. 13 Surface temperature anomaly resulting from the presence of a static sunshade.

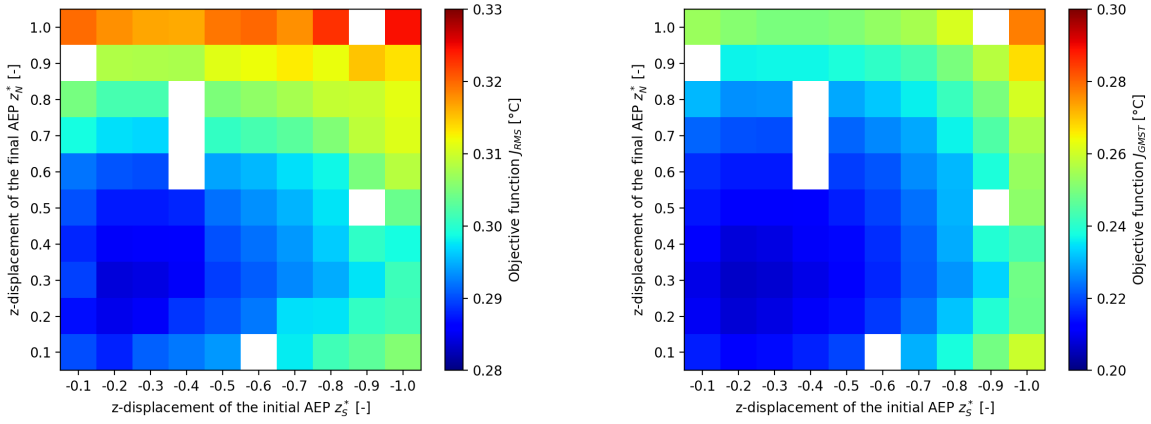

Fig. 14 Results of the grid search over the trajectory catalog for different combinations of z-displacement (z_S^* and z_N^*), with fixed departing dates of the transfers ($t_S = 60$ days, $t_N = 240$ days), performed for objective function J_{RMS} (left panel) and objective function J_{GMST} (right panel). White cells represent unfeasible transfer trajectories.

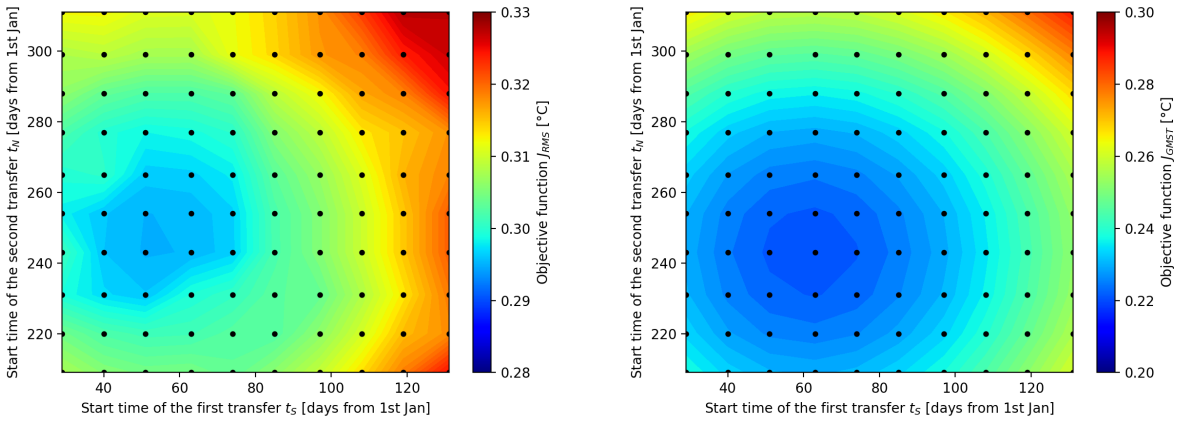

Fig. 15 Results of the grid search over the trajectory catalog for different combinations of start dates of the transfer (t_S and t_N), with fixed z-displacements ($z_S^* = -0.6R_\oplus$, $z_N^* = +0.6R_\oplus$), performed for objective function J_{RMS} (left panel) and objective function J_{GMST} (right panel). White cells represent unconverged transfer trajectories.

(z_S^* and z_N^*). A typical transfer trajectory resulting from the optimal control problem presented in Sec. VIII.A was already shown in Fig. 11. Instead, the second grid search fixes the initial and final z-displacement of the trajectory ($z_S^* = -0.6R_\oplus$, $z_N^* = 0.6R_\oplus$) while varying the dates when the sunshade departs from the AEPs. For each combination of z-displacement and departing dates, all the steps described in Fig. 2 are carried out: the time-optimal trajectory is found, the shading pattern is computed, and a climate simulation with the GREB model is performed, resulting in the evaluation of two metrics (the objective functions J_{RMS} and J_{GMST}). The objective function J_{polar} is not considered for the grid searches. The results are reported in Fig. 14 for the first grid search and in Fig. 15 for the second grid search.

Before analyzing the results, it should be mentioned that white cells in the figures correspond to unconverged transfers. Such trajectories are not unfeasible; on the contrary, it was verified that the optimizer is very sensitive to the number of collocation points. Therefore, the apparent unfeasibility could be solved using an iterative trial-and-error approach to a change in the number of collocation points.

Looking at Fig. 14, it can be noticed that the first type of grid search shows similar results for both objectives. The best-performing trajectories are found in the region described by $-0.3 \leqslant z_S^* \leqslant -0.2$ and $+0.2 \leqslant z_N^* \leqslant +0.3$, with the objective function gradually increasing for absolute displacement values larger than 0.3. It can also be noticed that the objective function J_{RMS} is slightly less sensitive to changes in the z-displacements with respect to objective J_{GMST}. Finally, Fig. 14 confirms again that a static shade with no vertical displacement is not the optimal solution to minimize temperature anomalies.

Observing the results from the second grid search, reported in Fig. 15, it is possible to see some differences between the two objective functions. For objective function J_{RMS}, the best performing region is found at $40 < t_S < 60$ days and $240 < t_N < 260$ days; for objective function J_{GMST}, which shows a more regular behavior with respect to J_{RMS}, the best performing region is located at roughly $50 < t_S < 70$ days and $230 < t_N < 250$ days. As a reference, the equinoxes occur around day 79 (March 20$^{\text{th}}$) and day 266 (September 22$^{\text{nd}}$). The transfer trajectory takes between 40 and 50 days to complete. If J_{RMS} is used as objective, the asymmetry mentioned in Sec. IX.A appears as expected. This pattern confirms that the sunshade should spend more time over the northern hemisphere and less over the southern hemisphere. It is interesting to notice that, when objective function J_{GMST} is used, the figure looks rather symmetric. This is because the GMST gives relatively more weight to equatorial regions than to polar regions; therefore, the motion of the sunshade closely follows the apparent oscillation of the Earth's spinning axis, giving less weight to temperature anomalies at higher latitudes. In addition, the best performing regions for J_{RMS} show that the values of t_S and t_N are more spread apart compared to the grid search for J_{GMST}, meaning that the sunshade spends more time over the northern hemisphere, as expected. Finally, objectives J_{RMS} and J_{GMST} seem to be more sensitive to the z-displacement than to the departing dates, as it can be seen from the range of the colorbar in the contour plots in Fig. 14 and Fig. 15.

The two grid searches described above allow to restrict the search space for the heuristic optimization process. The new boundaries of the search space that will be used to solve the optimization problems are reported in Table 3.

Table 3 Boundaries of the search space for the single-objective optimization problem (GMST).

Variable	Lower boundary	Upper boundary	Unit
z_S^*	-0.5	0.0	–
z_N^*	0.0	0.5	–
t_S	30	70	days from January 1st
t_N	230	270	days from January 1st

C. Optimization of the sunshade's motion

The results of the single-objective optimization problems are presented in the following subsections: Sec. IX.C.1 when optimizing for J_{RMS}, Sec. IX.C.2 when optimizing for J_{GMST}, and Sec. IX.C.3 when optimizing for J_{polar}. It is noted again that, for all optimization problems, the search space is limited to the values reported in Table 3. The results reported in this section are obtained by initializing the population with a seed value equal to 20151017.

1. Root Mean Squares (J_{RMS})

Objective function J_{RMS} highlights the latitudinal differences in the surface temperature anomalies. The evolution of the fitness of the best individual ("champion") of the population is reported in Fig. 17, while the independent variables corresponding to the optimal solution are reported in Table 4. The value of the objective at the last evolution is $J_{\text{RMS}} = 0.2837\,^{\circ}\text{C}$ and the resulting temperature anomaly distribution is very similar to the one shown in Fig. 16. It can be noticed that the optimizer struggles to significantly improve the value of the objective function.

More generally, comparing the results of this subsection with the ones presented in Sec. IX.C.2 suggests that the chosen metrics have a relatively low sensitivity with respect to the selected independent variables. This is mainly caused by the fact that the shade cast on the Earth does not change significantly, coupled with the inherent complexity of the Earth's climate system and the non-linearity of the problem. An extensive comparison of the optimization results and of other climate scenarios presented in the paper (reference scenario, without a shade, and with a static shade) is summarized in Table 4.

2. Global Mean Surface Temperature (J_{GMST})

The objective function used in this section is J_{GMST}, therefore the optimal trajectory in terms of GMST is searched for. This objective function is inherently a global metric. The evolution of the fitness of the best individual ("champion") of the population is reported in Fig. 17, while the independent variables corresponding to the optimal solution are reported in Table 4. The value of the objective at the last evolution is $J_{\text{GMST}} = 0.2061\,^{\circ}\text{C}$.

It can be noticed that the optimal solution obtained when optimizing for J_{RMS} and the optimal solution obtained when optimizing for J_{GMST} produce comparable values of the RMS. The possible causes of this have been already mentioned in the previous paragraphs. However, the independent variables reported in Table 4, in particular the values of the vertical displacement, z_S^* and z_N^*, indicate that the sunshade tends to shade the tropical regions less. Indeed, the vertical displacement is greater when optimizing for J_{RMS}, as the optimizer focuses on minimizing latitudinal temperature anomalies (i.e., casting more shade on the poles), rather than on a global metric (GMST). In addition, When computing the value for J_{GMST} for the trajectory obtained when optimizing for J_{RMS}, it can be noticed how the value of J_{GMST} is slightly higher with respect to the optimal value computed when optimizing for J_{GMST}. This can be explained with the fact that relatively less shade is cast on the equatorial regions that have the biggest influence on the objective function J_{GMST}.

Furthermore, the improvement of the objective function, J_{GMST}, across 20 generations is relatively small. This is due to a number of factors: firstly, the search space was already constrained based on the findings of the grid search explained in the previous subsection; secondly, the optimization settings (population size and number of generations) are severely limited by the runtime. In addition, given the entity of the results obtained, one could wonder whether it is worth changing the location of the sunshade, in terms of operational costs and complexity. However, this is beyond the scope of this work.

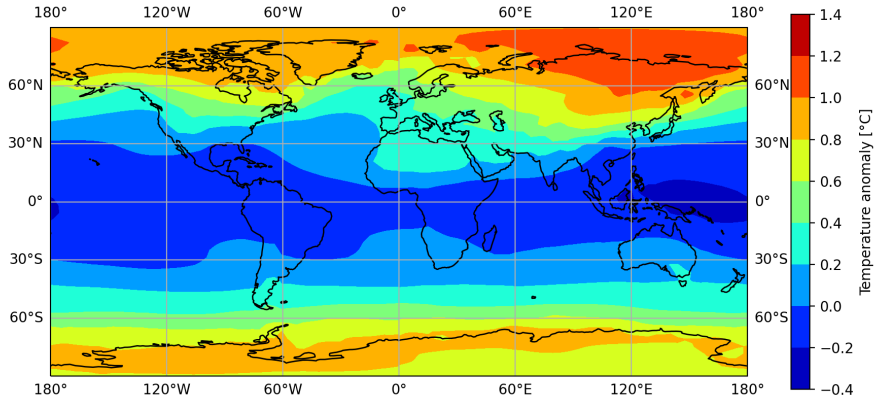

Fig. 16 Surface temperature anomaly resulting from the presence of a dynamic sunshade.

3. Polar Mean Surface Temperature (J_{polar})

The objective function J_{polar} forces the optimizer to focus on polar regions only. The evolution of the fitness of the best individual ("champion") of the population is reported in Fig. 17, while the independent variables corresponding to the optimal solution are reported in Table 4. The value of the objective at the last evolution is $J_{\text{polar}} = 0.9010\,^{\circ}\text{C}$ and the resulting temperature anomaly distribution is very similar to the one shown in Fig. 16. As a reference, the temperature anomaly of a static shade over the polar regions is $J^{\text{static}}_{\text{polar}} = 0.96\,^{\circ}\text{C}$. Therefore, this is another improvement with respect to the static shade. In addition, it can be observed that the reduction in polar temperature anomaly is two orders of magnitude greater than in global temperature anomaly. Again, as stated in Sec. IX.C.1, the values of the objectives do not differ significantly, but it can be noticed how the vertical displacement of the shade is higher than when optimizing for J_{RMS} and J_{GMST}. This was expected, as the objective function is solely focused on the surface temperature anomaly in the polar regions. It is interesting to notice how the vertical displacement, although greater than in the other cases, is limited to roughly $|z| < 0.32\,R_{\oplus}$, while larger values could have been predicted. This can be explained by two effects. Firstly, modeling solar radiation with limb darkening means that the center of the Sun should be shaded more than its limbs. Without solar limb darkening, the shade would be placed closer to the line connecting the Earth's pole to the center of the Sun. Secondly, it must be reminded that solar radiation is not the only source of climate forcing; internal energy exchanges through oceans and the atmosphere play a role as well, as explained in Sec. VII. Therefore, in order to minimize the surface temperature anomaly in a given region, casting a shade only on that area is not sufficient, as other regions would have a greater surface temperature, which would warm the target region by atmospheric energy transport (advection and diffusion). Although this explanation is greatly simplified, this result is another proof of the complexity of the climate system and of the non-linearity of the problem tackled in this paper.

4. Comparison

In Fig. 18 the vertical displacements of the optimal trajectories found in Sec. IX.C.2 through Sec. IX.C.3 are reported. All the features previously explained can be noticed: the vertical displacement is minimum when optimizing for J_{GMST}, increases for J_{RMS}, and is maximum for J_{polar}. Similarly, the cumulative transfer time decreases in the same order (J_{GMST}, J_{RMS}, and J_{polar}). This means, as expected, that the optimal trajectory found for J_{polar} spends more time at the equilibrium points to shade the polar regions, while the opposite is true for J_{GMST}. This is however not true for the second transfer, where the solution for J_{RMS} actually stays at the equilibrium point for longer. The reason for this was not exactly understood, but it may be simply caused by the optimization settings.

In addition, Fig. 18 shows another relevant feature that was already observed in Sec. IX.B. For the first transfer (from below to above the ecliptic plane), the sunshade crosses the ecliptic plane almost exactly at the equinox (dashed vertical line in the figure). However, for the second transfer, this is not the case: it can be noticed that the sunshade spends more time above the northern hemisphere, therefore the crossing of the ecliptic plane is delayed and happens only after the equinox (between 5 and 10 days later). This feature confirms the findings observed in Fig. 15, further clarifying the fact that the northern hemisphere should be shaded more than the southern hemisphere. The reason for

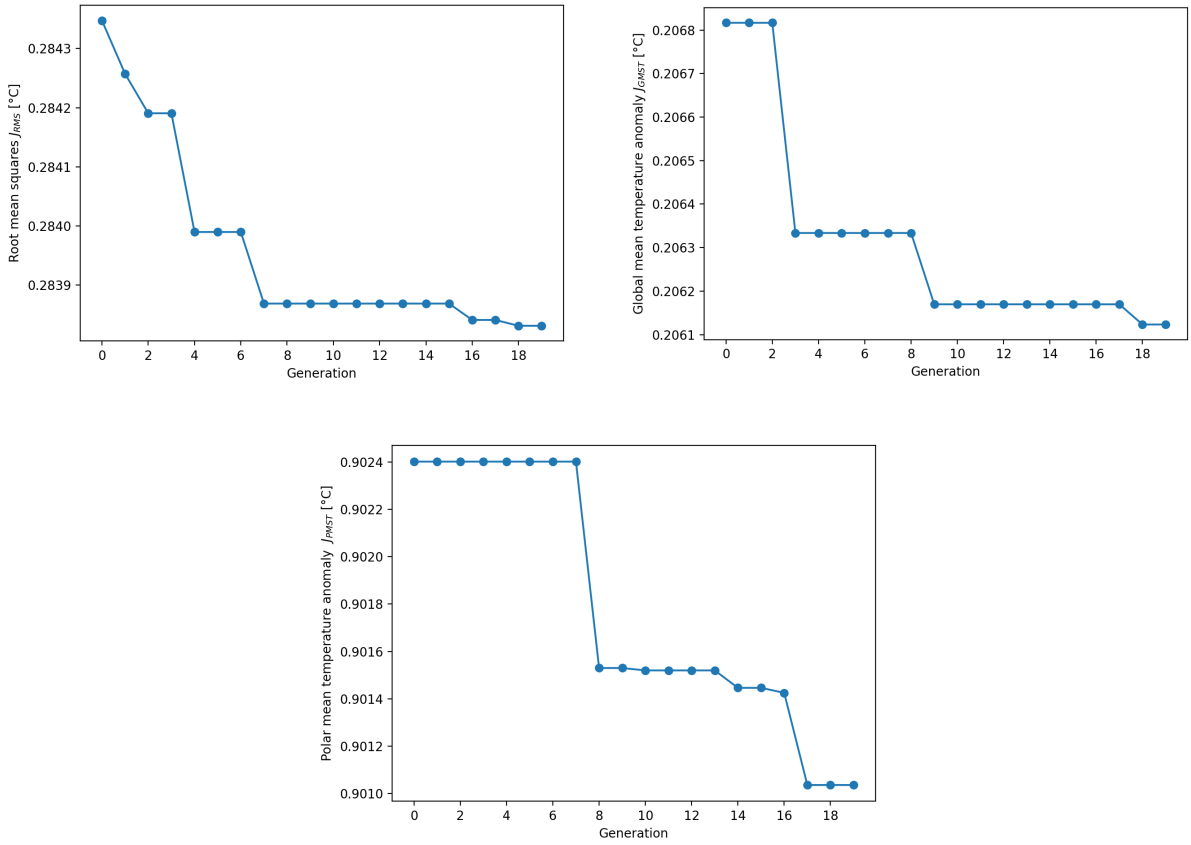

Fig. 17 Evolution of the best individual in the population when optimizing for J_{RMS} (top left panel), J_{GMST} (top right panel), and J_{PMST} (bottom panel).

this is related to the ocean/land ratio and was already explained in Sec. IX.B.

X. Conclusions

In this paper, the optimal trajectory of a planetary sunshade placed in the vicinity of the Sun-Earth L_1 point was investigated to minimize regional imbalances observed for a static shade at L_1. The sunshade was modeled as an ideal solar sail in the dynamical framework of the Circular Restricted Three-Body Problem. A simplified climate model, GREB [36], was employed to evaluate the climatic evolution under different shading conditions. The Global Mean Surface Temperature (GMST) of the reference scenario (pre-industrial levels of atmospheric CO_2, equal to 340 ppm, without the sunshade) found is $\bar{T}^{\mathrm{global}}_{\mathrm{ref}} = 13.92\ ^{\circ}\mathrm{C}$. With an increased amount of atmospheric CO_2 (680 ppm), the resulting GMST is $\bar{T}^{\mathrm{global}}_{2xCO2} = 16.39\ ^{\circ}\mathrm{C}$. It was found that a static shade with a fixed radius of 1434 km placed at a displaced equilibrium point on the ecliptic plane at a distance of $2.44 \cdot 10^6$ km from the Earth can reduce the GMST to $\bar{T}^{\mathrm{global}}_{\mathrm{geo}} = 14.15\ ^{\circ}\mathrm{C}$. While a dynamic shade improves the GMST by only $0.02\ ^{\circ}\mathrm{C}$ to $\bar{T}^{\mathrm{global}}_{\mathrm{geo}} = 14.13\ ^{\circ}\mathrm{C}$, it reduces the Polar Mean Surface Temperature (PMST) by $0.06\ ^{\circ}\mathrm{C}$. In addition, a dynamic shade delivers an improvement in latitudinal imbalances compared to a static shade – quantified through the Root Mean Squares (RMS) of the latitudinal temperature anomaly distribution – from $0.3032\ ^{\circ}\mathrm{C}$ to $0.2837\ ^{\circ}\mathrm{C}$, representing a 6.4% improvement. The most promising trajectory solutions move periodically between Artificial Equilibrium Points (AEPs) located at roughly 0.3 Earth radii above and 0.3 Earth radii below the ecliptic plane, with a slightly larger vertical displacement above the ecliptic plane. The optimal starting dates of the transfers are close to $t_S = 56$ days and $t_N = 250$ days for the transfers (from below to above the ecliptic plane and vice versa, respectively). While the trajectory found when optimizing for the GMST anomaly is almost symmetric in time and space, the optimal trajectory to minimize the PMST anomaly moves between

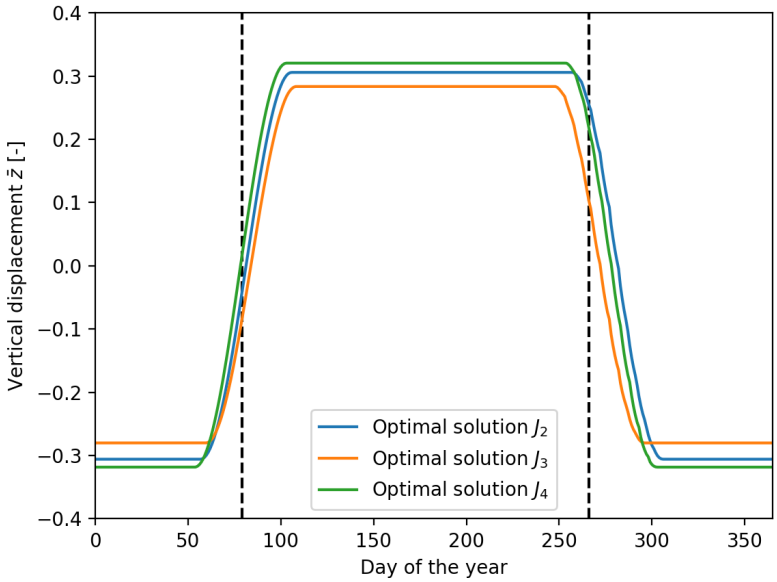

Fig. 18 Vertical displacement profile of the optimal solutions plotted against the day of the year.

AEPs displaced further above and below the ecliptic plane and remains there longer. This way, more shade can be cast over the polar regions; this, however, comes at the cost of a slightly higher GMST anomaly, since less shade is cast over tropical regions. In addition, it was observed that the northern hemisphere is shaded more and for longer than the southern hemisphere. This result can be explained through the imbalance in the land-to-ocean ratio, which is greater in the northern hemisphere, coupled with the higher heat storage capacity of oceans with respect to the land.

The results found in this paper highlight the benefits of a dynamic shade over a static one. So far, this is one of the only two studies tackling the problem of a dynamic sunshade for geoengineering purposes, together with Reference [33]. This study also employs and validates a trajectory design approach that has never been considered before in the context of space-based geoengineering. Therefore, this work constitutes a unique contribution to the research body concerned with space-based solar geoengineering solutions and its effects on the Earth's climate.

Acknowledgments

An acknowledgement goes to the FAST University Fund from Delft University of Technology for providing financial support to present this paper at the ASCEND conference 2022.

Table 4 Summary of the results. Highlighted cells show the objective function for each optimization problem.

Case	z_S^*	z_N^*	t_S	t_N	$\bar{T}^{\text{global}}$ [$^\circ C$]	$\bar{T}^{\text{polar}}$ [$^\circ C$]	J_{RMS} [$^\circ C$]	J_{GMST} [$^\circ C$]	J_{polar} [$^\circ C$]
Reference	–	–	–	–	13.92	−18.42	–	–	–
No shade	–	–	–	–	16.39	−15.44	2.5049	2.4711	2.9795
Static shade	0	0	0	0	14.15	−17.46	0.3032	0.2318	0.9633
Optimal J_2	−0.3059	+0.3058	56.80	254.99	14.13	−17.52	0.2837	0.2062	0.9013
Optimal J_3	−0.2801	+0.2835	59.71	245.59	14.13	−17.52	0.2837	0.2061	0.9017
Optimal J_4	−0.31841	+0.32050	53.74	251.38	14.13	−17.52	0.2840	0.2067	0.9010

References

[1] IPCC, Mayer, L., and Pachauri, R. K. (eds.), *Climate change 2014: synthesis report*, Intergovernmental Panel on Climate Change, Geneva, Switzerland, 2015.

[2] "Geoengineering the climate : science, governance and uncertainty," Tech. rep., Royal Society, 2009.

[3] Keith, D. W., "Why Capture CO $_2$ from the Atmosphere?" *Science*, Vol. 325, No. 5948, 2009, pp. 1654–1655. https://doi.org/10.1126/science.1175680, URL https://www.science.org/doi/10.1126/science.1175680.

[4] Rasch, P. J., Tilmes, S., Turco, R. P., Robock, A., Oman, L., Chen, C.-C. J., Stenchikov, G. L., and Garcia, R. R., "An overview of geoengineering of climate using stratospheric sulphate aerosols," *Philosophical Transactions of the Royal Society A: Mathematical, Physical and Engineering Sciences*, Vol. 366, No. 1882, 2008, pp. 4007–4037. https://doi.org/10.1098/rsta.2008.0131, URL https://royalsocietypublishing.org/doi/10.1098/rsta.2008.0131.

[5] Lenton, T. M., Held, H., Kriegler, E., Hall, J. W., Lucht, W., Rahmstorf, S., and Schellnhuber, H. J., "Tipping elements in the Earth's climate system," *Proceedings of the National Academy of Sciences*, Vol. 105, No. 6, 2008, pp. 1786–1793. https://doi.org/10.1073/pnas.0705414105, URL https://pnas.org/doi/full/10.1073/pnas.0705414105.

[6] McInnes, C. R., "Minimum mass solar shield for terrestrial climate control," *JBIS - Journal of the British Interplanetary Society*, Vol. 55, No. 9-10, 2002.

[7] Baum, C. M., Low, S., and Sovacool, B. K., "Between the sun and us: Expert perceptions on the innovation, policy, and deep uncertainties of space-based solar geoengineering," *Renewable and Sustainable Energy Reviews*, Vol. 158, 2022, p. 112179. https://doi.org/10.1016/j.rser.2022.112179, URL https://linkinghub.elsevier.com/retrieve/pii/S1364032122001046.

[8] Govindasamy, B., and Caldeira, K., "Geoengineering Earth's radiation balance to mitigate CO2-induced climate change," *Geophysical Research Letters*, Vol. 27, No. 14, 2000, pp. 2141–2144. https://doi.org/10.1029/1999GL006086, publisher: American Geophysical Union.

[9] Govindasamy, B., Caldeira, K., and Duffy, P. B., "Geoengineering Earth's radiation balance to mitigate climate change from a quadrupling of CO2," *Global and Planetary Change*, Vol. 37, No. 1-2, 2003, pp. 157–168. https://doi.org/10.1016/S0921-8181(02)00195-9, publisher: Elsevier B.V.

[10] Robock, A., Oman, L., and Stenchikov, G. L., "Regional climate responses to geoengineering with tropical and Arctic SO2 injections," *Journal of Geophysical Research*, Vol. 113, No. D16, 2008, p. D16101. https://doi.org/10.1029/2008JD010050, URL http://doi.wiley.com/10.1029/2008JD010050.

[11] Ricke, K. L., Morgan, M. G., and Allen, M. R., "Regional climate response to solar-radiation management," *Nature Geoscience*, Vol. 3, No. 8, 2010, pp. 537–541. https://doi.org/10.1038/ngeo915, URL http://www.nature.com/articles/ngeo915.

[12] Caldeira, K., and Wood, L., "Global and Arctic climate engineering: numerical model studies," *Philosophical Transactions of the Royal Society A: Mathematical, Physical and Engineering Sciences*, Vol. 366, No. 1882, 2008, pp. 4039–4056. https://doi.org/10.1098/rsta.2008.0132, URL https://royalsocietypublishing.org/doi/10.1098/rsta.2008.0132.

[13] Govindasamy, B., Thompson, S., Duffy, P. B., Caldeira, K., and Delire, C., "Impact of geoengineering schemes on the terrestrial biosphere," *Geophysical Research Letters*, Vol. 29, No. 22, 2002, pp. 18–1–18–4. https://doi.org/10.1029/2002gl015911, publisher: American Geophysical Union.

[14] Bala, G., Duffy, P. B., and Taylor, K. E., "Impact of geoengineering schemes on the global hydrological cycle," *Proceedings of the National Academy of Sciences*, Vol. 105, No. 22, 2008, pp. 7664–7669. https://doi.org/10.1073/pnas.0711648105, URL http://www.pnas.org/cgi/doi/10.1073/pnas.0711648105.

[15] Matthews, H. D., Caldeira, K., and Karl, D. M., "Transient climate-carbon simulations of planetary geoengineering," *Proceedings of the National Academy of Sciences*, Vol. 104, No. 24, 2007, pp. 9949–9954. URL www.pnas.orgcgidoi10.1073pnas.0700419104.

[16] Moreno-Cruz, J. B., Ricke, K. L., and Keith, D. W., "A simple model to account for regional inequalities in the effectiveness of solar radiation management," *Climatic Change*, Vol. 110, No. 3-4, 2012, pp. 649–668. https://doi.org/10.1007/s10584-011-0103-z.

[17] Ban-Weiss, G. A., and Caldeira, K., "Geoengineering as an optimization problem," *Environmental Research Letters*, Vol. 5, No. 3, 2010. https://doi.org/10.1088/1748-9326/5/3/034009, publisher: Institute of Physics Publishing.

[18] MacMartin, D. G., Keith, D. W., Kravitz, B., and Caldeira, K., "Management of trade-offs in geoengineering through optimal choice of non-uniform radiative forcing," *Nature Climate Change*, Vol. 3, No. 4, 2013, pp. 365–368. https://doi.org/10.1038/nclimate1722.

[19] Early, J. T., "Space-based solar shield to offset greenhouse effect," *Journal of the British Interplanetary Society*, Vol. 42, 1989, pp. 567–569.

[20] Hudson, H., "A space parasol as a countermeasure against the greenhouse effect," *Journal of the British Interplanetary Society*, Vol. 44, 1991, p. 139.

[21] Mautner, M. N., "Deep-space solar screens against climatic warming: technical and research requirements," *Proceedings of the Third Pacific Basin International Symposium on Advances in Space Sciences Technology and its Applications (PISSTA)*, 1989. URL https://www.researchgate.net/publication/321712294.

[22] Mautner, M., "A space-based solar screen against climatic warming," *Journal of the British Interplanetary Society*, Vol. 44, No. 3, 1991.

[23] Pearson, J., Oldson, J., and Levin, E., "Earth rings for planetary environment control," *Acta Astronautica*, Vol. 58, No. 1, 2006. https://doi.org/10.1016/j.actaastro.2005.03.071.

[24] Struck, C., "The Feasibility of Shading the Greenhouse with Dust Clouds at the Stable Lunar Lagrange Points," *Journal of the British Interplanetary Society*, Vol. 60, 2007.

[25] Bewick, R., Sanchez, J. P., and McInnes, C. R., "The feasibility of using an L 1 positioned dust cloud as a method of space-based geoengineering," *Advances in Space Research*, Vol. 49, No. 7, 2012, pp. 1212–1228. https://doi.org/10.1016/j.asr.2012.01.010, publisher: Elsevier Ltd.

[26] Roy, K. I., "Solar sails: An answer to Global Warming?" *AIP Conference Proceedings*, Vol. 552, AIP, Albuquerque, New Mexico, 2001, pp. 413–418. https://doi.org/10.1063/1.1357956, URL http://aip.scitation.org/doi/abs/10.1063/1.1357956, iSSN: 0094243X.

[27] Angel, R., "Feasibility of cooling the Earth with a cloud of small spacecraft near the inner Langrange point (L1)," *Proceedings of the National Academy of Sciences of the United States of America*, Vol. 103, No. 46, 2006. https://doi.org/10.1073/pnas.0608163103.

[28] Biggs, J. D., and McInnes, C. R., "Passive Orbit Control for Space-Based Geo-eEngineering," *Journal of Guidance, Control, and Dynamics*, Vol. 33, No. 3, 2010, pp. 1017–1020. https://doi.org/10.2514/1.46054, URL https://arc.aiaa.org/doi/10.2514/1.46054.

[29] Seeley, J. T., Lutsko, N. J., and Keith, D. W., "Designing a Radiative Antidote to CO2," *Geophysical Research Letters*, Vol. 48, No. 1, 2021. https://doi.org/10.1029/2020GL090876, URL https://onlinelibrary.wiley.com/doi/10.1029/2020GL090876.

[30] Fuglesang, C., and de Herreros Miciano, M. G., "Realistic sunshade system at L1 for global temperature control," *Acta Astronautica*, Vol. 186, 2021, pp. 269–279. https://doi.org/10.1016/j.actaastro.2021.04.035, URL https://linkinghub.elsevier.com/retrieve/pii/S0094576521001995.

[31] Kosugi, T., "Role of sunshades in space as a climate control option," *Acta Astronautica*, Vol. 67, No. 1-2, 2010, pp. 241–253. https://doi.org/10.1016/j.actaastro.2010.02.009.

[32] Lunt, D. J., Ridgwell, A., Valdes, P. J., and Seale, A., ""Sunshade World": A fully coupled GCM evaluation of the climatic impacts of geoengineering," *Geophysical Research Letters*, Vol. 35, No. 12, 2008. https://doi.org/10.1029/2008GL033674, publisher: American Geophysical Union.

[33] Sánchez, J.-P., and McInnes, C. R., "Optimal Sunshade Configurations for Space-Based Geoengineering near the Sun-Earth L1 Point," *PLOS ONE*, Vol. 10, No. 8, 2015, p. e0136648. https://doi.org/10.1371/journal.pone.0136648, URL https://dx.plos.org/10.1371/journal.pone.0136648.

[34] McInnes, C. R., McDonald, A. J. C., Simmons, J. F. L., and MacDonald, E. W., "Solar sail parking in restricted three-body systems," *Journal of Guidance, Control, and Dynamics*, Vol. 17, No. 2, 1994, pp. 399–406. https://doi.org/10.2514/3.21211, URL https://arc.aiaa.org/doi/10.2514/3.21211.

[35] McInnes, C. R., *Solar sailing: technology, dynamics and mission applications*, Springer-Praxis series in space science and technology, Springer [u.a.], London, 1999. OCLC: 246336919.

[36] Dommenget, D., and Flöter, J., "Conceptual understanding of climate change with a globally resolved energy balance model," *Climate Dynamics*, Vol. 37, No. 11-12, 2011, pp. 2143–2165. https://doi.org/10.1007/s00382-011-1026-0, URL http://link.springer.com/10.1007/s00382-011-1026-0.

[37] Heiligers, J. M., and McInnes, C. R., "Agile solar sailing in three-body problem: Motion between artificial equilibrium points," International Astronautical Federation, Beijing, China, 2013.

[38] Lissauer, J. J., and De Pater, I., *Fundamental Planetary Science*, Cambridge University Press, USA, 2013.

[39] Szebehely, V. G., *Theory of orbits: the restricted problem of three bodies*, Academic Press, 1967.

[40] Heiligers, J., Vergaaij, M., and Ceriotti, M., "End-to-end trajectory design for a solar-sail-only pole-sitter at Venus, Earth, and Mars," *Advances in Space Research*, Vol. 67, No. 9, 2021, pp. 2995–3011. https://doi.org/10.1016/j.asr.2020.06.011, URL https://linkinghub.elsevier.com/retrieve/pii/S0273117720304130.

[41] Nicodemus, F. E., "Radiance," *American Journal of Physics*, Vol. 31, No. 5, 1963, pp. 368–377. https://doi.org/10.1119/1.1969512, URL http://aapt.scitation.org/doi/10.1119/1.1969512.

[42] Kopp, G., and Lean, J. L., "A new, lower value of total solar irradiance: Evidence and climate significance: FRONTIER," *Geophysical Research Letters*, Vol. 38, No. 1, 2011, pp. n/a–n/a. https://doi.org/10.1029/2010GL045777, URL http://doi.wiley.com/10.1029/2010GL045777.

[43] Hartmann, D. L., *Global physical climatology*, No. v. 56 in International geophysics, Academic Press, San Diego, 1994.

[44] Vasquez Padilla, Ricardo, "Simplified Methodology for Designing Parabolic Trough Solar Power Plants," Ph.D. thesis, USF Tampa, Tampa, Florida, 2011. URL https://digitalcommons.usf.edu/etd/3390.

[45] Escobal, P. R., and Robertson, R. A., "Lunar eclipse of a satellite of the earth." *Journal of Spacecraft and Rockets*, Vol. 4, No. 4, 1967, pp. 538–540. https://doi.org/10.2514/3.28903, URL https://arc.aiaa.org/doi/10.2514/3.28903.

[46] Vallado, D. A., and McClain, W. D., *Fundamentals of astrodynamics and applications*, 4$^{\text{th}}$ ed., No. 21 in Space technology library, Microcosm Press, Hawthorne, Calif, 2013.

[47] Wertz, J. R., *Mission geometry: orbit and constellation design and management ; spacecraft orbit and attitude systems*, No. 13 in Space technology library, Microcosm Press, El Segundo, Calif, 2001.

[48] Pierce, A., and Slaughter, C., "Solar limb darkening," *Solar Physics*, Vol. 51, No. 1, 1977. https://doi.org/10.1007/BF00240442, URL http://link.springer.com/10.1007/BF00240442.

[49] Neckel, H., and Labs, D., "Solar limb darkening 1986–1990 (303 to 1099 nm)," *Solar Physics*, Vol. 153, No. 1-2, 1994, pp. 91–114. https://doi.org/10.1007/BF00712494, URL http://link.springer.com/10.1007/BF00712494.

[50] Cox, A. N., and Cox, A. N., *Allen's Astrophysical Quantities*, 2002. URL https://link.springer.com/book/10.1007/978-1-4612-7037-9, oCLC: 1058941068.

[51] Budyko, M. I., "The effect of solar radiation variations on the climate of the Earth," *Tellus*, Vol. 21, No. 5, 1969, pp. 611–619. https://doi.org/10.1111/j.2153-3490.1969.tb00466.x, URL http://tellusa.net/index.php/tellusa/article/view/10109.

[52] Sellers, W. D., "A global climatic model based on the energy balance of the Earth-Atmosphere system," *Journal of Applied Meteorology*, Vol. 8, 1969, pp. 392–400.

[53] Petoukhov, V., Claussen, M., Berger, A., Crucifix, M., Eby, M., Eliseev, A. V., Fichefet, T., Ganopolski, A., Goosse, H., Kamenkovich, I., Mokhov, I. I., Montoya, M., Mysak, L. A., Sokolov, A., Stone, P., Wang, Z., and Weaver, A. J., "EMIC Intercomparison Project (EMIP–CO2): comparative analysis of EMIC simulations of climate, and of equilibrium and transient responses to atmospheric CO2 doubling," *Climate Dynamics*, Vol. 25, No. 4, 2005, pp. 363–385. https://doi.org/10.1007/s00382-005-0042-3, URL http://link.springer.com/10.1007/s00382-005-0042-3.

[54] Meehl, G. A., Covey, C., Delworth, T., Latif, M., McAvaney, B., Mitchell, J. F. B., Stouffer, R. J., and Taylor, K. E., "THE WCRP CMIP3 Multimodel Dataset: A New Era in Climate Change Research," *Bulletin of the American Meteorological Society*, Vol. 88, No. 9, 2007, pp. 1383–1394. https://doi.org/10.1175/BAMS-88-9-1383, URL https://journals.ametsoc.org/doi/10.1175/BAMS-88-9-1383.

[55] Nicholls, Z. R. J., Meinshausen, M., Lewis, J., Gieseke, R., Dommenget, D., Dorheim, K., Fan, C.-S., Fuglestvedt, J. S., Gasser, T., Golüke, U., Goodwin, P., Hartin, C., Hope, A. P., Kriegler, E., Leach, N. J., Marchegiani, D., McBride, L. A., Quilcaille, Y., Rogelj, J., Salawitch, R. J., Samset, B. H., Sandstad, M., Shiklomanov, A. N., Skeie, R. B., Smith, C. J., Smith, S., Tanaka, K., Tsutsui, J., and Xie, Z., "Reduced Complexity Model Intercomparison Project Phase 1: introduction and evaluation of global-mean temperature response," *Geoscientific Model Development*, Vol. 13, No. 11, 2020, pp. 5175–5190. https://doi.org/10.5194/gmd-13-5175-2020, URL https://gmd.copernicus.org/articles/13/5175/2020/.

[56] Betts, J. T., "Survey of numerical methods for trajectory optimization," *Journal of guidance, control, and dynamics*, Vol. 21, No. 2, 1998, pp. 193–207.

[57] Betts, J. T., *Practical methods for optimal control using nonlinear programming*, Advances in design and control, Society for Industrial and Applied Mathematics, Philadelphia, PA, 2001.

[58] Biegler, L. T., *Nonlinear programming: concepts, algorithms, and applications to chemical processes*, MOS-SIAM series on optimization, Society for Industrial and Applied Mathematics : Mathematical Programming Society, Philadelphia, 2010.

[59] Bynum, M. L., Hackebeil, G. A., Hart, W. E., Laird, C. D., Nicholson, B. L., Siirola, J. D., Watson, J.-P., and Woodruff, D. L., *Pyomo — Optimization Modeling in Python*, Springer Optimization and Its Applications, Vol. 67, Springer International Publishing, Cham, 2021. https://doi.org/10.1007/978-3-030-68928-5, URL http://link.springer.com/10.1007/978-3-030-68928-5.

[60] Wächter, A., and Biegler, L. T., "On the implementation of an interior-point filter line-search algorithm for large-scale nonlinear programming," *Mathematical Programming*, Vol. 106, No. 1, 2006, pp. 25–57. https://doi.org/10.1007/s10107-004-0559-y, URL http://link.springer.com/10.1007/s10107-004-0559-y.

[61] Hausfather, Z., Cowtan, K., Menne, M. J., and Williams, C. N., "Evaluating the impact of U.S. Historical Climatology Network homogenization using the U.S. Climate Reference Network," *Geophysical Research Letters*, Vol. 43, No. 4, 2016, pp. 1695–1701. https://doi.org/10.1002/2015GL067640, URL https://onlinelibrary.wiley.com/doi/10.1002/2015GL067640.

[62] Storn, R., and Price, K., "Differential Evolution – A Simple and Efficient Heuristic for global Optimization over Continuous Spaces," *Journal of Global Optimization*, Vol. 11, No. 4, 1997, pp. 341–359. https://doi.org/10.1023/A:1008202821328, URL http://link.springer.com/10.1023/A:1008202821328.

[63] Biscani, F., and Izzo, D., "A parallel global multiobjective framework for optimization: pagmo," *Journal of Open Source Software*, Vol. 5, No. 53, 2020, p. 2338.

[64] Marshall, J., and Plumb, R. A., *Atmosphere, ocean, and climate dynamics: an introductory text*, No. v. 93 in International geophysics series, Elsevier Academic Press, Amsterdam ; [Burlington, MA], 2008. OCLC: ocn166317541.